Icarus 282 (2017) 237–259

Contents lists available at ScienceDirect

Icarus

journal homepage: www.elsevier.com/locate/icarus

Structure and density of Callisto's atmosphere from a fluid-kinetic model of its ionosphere: Comparison with Hubble Space Telescope and Galileo observations

Oliver Hartkorn[a,*], Joachim Saur[a], Darrell F. Strobel[b]

[a] Institute of Geophysics and Meteorology, University of Cologne, Pohligstr. 3, 50969 Cologne, Germany
[b] Department of Earth and Planetary Sciences, Johns Hopkins University, MD 21210, Baltimore, USA

ARTICLE INFO

Article history:
Received 18 January 2016
Revised 19 August 2016
Accepted 9 September 2016
Available online 30 September 2016

Keywords:
Callisto
Ionospheres
Satellites
atmospheres
Atmospheres
structure
Atmospheres
composition

ABSTRACT

We develop a model of the ionospheric electron population of Jupiter's moon Callisto using a prescribed neutral atmosphere composed of O_2, CO_2 and H_2O. A kinetic description of ionospheric suprathermal electrons coupled with a fluid description of ionospheric thermal electrons is well suited to jointly analyze and interpret observations of electron density and atmospheric UV emission. Accordingly, we calculate the electron energy distribution function at each point in the ionosphere by solving a coupled set of equations consisting of the Boltzmann equation for suprathermal electrons and the continuity and energy equation for thermal electrons. We assume a stationary balance between local sources and sinks of electrons and electron energy. Electron transport within the ionosphere is neglected, since collision time scales are shorter than transport time scales in the region of Callisto's ionosphere where the major concentrations of electrons is located and the major part of the atmospheric UV emission is generated. We consider photoionization, which is the dominant ionospheric electron source, and secondary ionization from collisions of photoelectrons with neutrals. Our calculations yield electron densities and electron impact generated UV emissions from Callisto's atmosphere. Comparing our modeled UV emission intensities with the Hubble Space Telescope observation of Cunningham et al. (2015) , we find that Callisto's atmosphere has a mean O_2 column density of $2.1^{+1.1}_{-1.1} \times 10^{19}$ m^{-2}. A joint comparison with this HST observation and radio occultation observations of Kliore et al. (2002) shows that Callisto's atmosphere possesses a day night asymmetry. We derive terminator O_2 column densities of $\sim 0.4 \times 10^{19}$ m^{-2}, for which we find subsolar O_2 column densities in the range of $2.4 - 9.8 \times 10^{19}$ m^{-2}. Our calculations also show that the electron density is very sensitive to the relative abundance of H_2O due to the thermal electron cooling by rotational state excitation of H_2O. For the efficiency of Callisto's atmospheric UV emission we find that on average one photon is emitted at OI λ135.6 nm per every 170 electron ion pairs generated and per every 60 electron ion pairs produced by secondary electron impact ionization.

1. Introduction

Recent observational progress on Callisto's atmosphere by Cunningham et al. (2015) and the upcoming JUICE mission (JUpiter ICy moons Explorer) have initiated further interest to better understand Callisto's atmosphere and plasma environment (e.g., Lindkvist et al., 2015; Vorburger et al., 2015; Liuzzo et al., 2015). Cunningham et al. (2015) presented possible evidence of an O_2 dominated atmosphere by measuring Callisto's atmospheric ultraviolet (UV) emission with the Hubble Space Telescope (HST). Kliore et al. (2002) proposed the existence of such an O_2 atmosphere on Callisto when they discovered an ionosphere using radio science measurements from the Galileo spacecraft.

The subject of our theoretical work is to further investigate and constrain the density and structure of Callisto's atmosphere. So far, there has been no theoretical study of Callisto's atmosphere ionosphere system that aims to understand and model the observations of Cunningham et al. (2015) and Kliore et al. (2002) simultaneously. For this purpose, we develop a model of Callisto's ionosphere describing the processes that maintain the ionosphere and its UV emission. We distinguish between thermal electrons forming the Maxwellian distributed bulk of ionospheric electrons

* Corresponding author.
E-mail address: ohartkor@uni-koeln.de (O. Hartkorn).

http://dx.doi.org/10.1016/j.icarus.2016.09.020

and suprathermal electrons forming the non-Maxwellian high energy tail (e.g., Stamnes and Rees, 1983). A kinetic description of the suprathermal electron population is required since its detailed characteristics strongly control the atmospheric UV emission. We aim to constrain structure and density of Callisto's atmosphere by varying a prescribed atmosphere composed of O_2, CO_2 and H_2O and using comparisons of model results with observations.

Up to now, CO_2 is the species of Callisto's atmosphere that has been observed with the most certainty. Carlson (1999) reported on measurements of the near-infrared mapping spectrograph of the Galileo spacecraft. This spectrograph detected limb emission from the 4.26 μm $\nu 3$ fundamental stretching band of CO_2 up to ~ 100 km above the surface and approximately at the equator and noon. In order to explain this observation, Carlson (1999) derived an atmospheric CO_2 column density of $0.80^{+0.48}_{-0.48} \times 10^{19}$ m^{-2}.

Later Kliore et al. (2002) detected an ionosphere at Callisto after the Galileo spacecraft had already found hints for an ionosphere-like plasma surrounding Callisto (Gurnett et al., 2000). In their study, Kliore et al. (2002) analyzed Galileo radio occultation measurements of flybys C-9, C-20, C-22 and C-23 providing electron density altitude profiles for an altitude range of 0–200 km. The authors derived peak ionospheric electron densities up to 4×10^{10} m^{-3} during entry observations of flyby C-22 and flyby C-23. They claimed that these ionospheric electron densities are too large to possibly originate only from the derived CO_2 atmosphere and suggested that O_2 is the major species of Callisto's atmosphere in analogy to Europa's atmosphere.

Kliore et al. (2002) provided also a first estimation of the density of the assumed O_2 atmosphere. They calculated an O_2 column density of $3–4 \times 10^{20}$ m^{-2} based on the altitudes of the electron density peaks from C-22 and C-23 and an electron energy independent local equilibrium model of the ionosphere. Since the Galileo spacecraft did not observe substantial ionosphere signals while the leading side was sunlit during C-9, the authors suggested that a substantial ionosphere could only be observed if the orbitally trailing side is sunlit as was the case during C-20, C-22 and C-23. They speculated that surface sputtering at the trailing side accompanied by photoionization might be a necessary precondition for the formation of a substantial atmosphere ionosphere system.

Before Cunningham et al. (2015) confirmed the existence of an O_2 atmosphere on Callisto Strobel et al. (2002) had reported HST observations with the Space Telescope Imaging Spectrograph (STIS). These HST/STIS observations, carried out in December 2001, did not show any oxygen signature from Callisto's atmosphere within the error bars. Based on these observations, Strobel et al. (2002) derived upper limits of about 10^{21} m^{-2} for the column densities of pure atmospheres of O_2, CO_2 and CO. The authors also discussed the interaction between Callisto and the upstream magnetospheric plasma: Due to the low strength of the Jovian magnetic field at Callisto's orbit of about 4–42 nT (Kivelson et al., 2004), the Pedersen conductance of Callisto's ionosphere is much larger than the Alfvén conductance such that the magnetospheric plasma is strongly diverted around the satellite. Therefore, Strobel et al. (2002) suggested that magnetospheric electron impact ionization is not the driving process of Callisto's ionosphere formation.

Finally, Cunningham et al. (2015) found UV emission from Callisto's atmosphere at OI λ130.4 and OI λ135.6 nm using the Cosmic Origins Spectrograph (COS) of HST. Note that these multiplets are the first direct observation of O-emission from Callisto's predicted O_2 atmosphere. Cunningham et al. (2015) benefited from the high sensitivity of the COS camera, which was installed on HST in May 2009. Confined to Callisto's disk, the brightness of the observed OI λ135.6 nm emission line is 3.17 ± 1.57 Rayleigh (R) and the brightness of the OI λ130.4 nm emission line is 3.32 ± 2.84 R. From the ratio of both multiplets, Cunningham et al. (2015) derived that Callisto's atmosphere is very likely O_2 dominated. In agreement with Strobel et al. (2002), they showed that photoionization is most likely the dominant driver of the ionosphere formation on Callisto's day side and photoelectrons predominately excite O_2 molecules and generate the observed atmospheric UV emission.

From the observed OI λ135.6 nm emission, Cunningham et al. (2015) calculated an atmospheric O_2 column density of $3.4^{+2.0}_{-1.8} \times 10^{19}$ m^{-2}. Their calculation is based on an approximation of the photoelectron impact ionization rate using the study of Wedlund et al. (2011). Further, they used results of an early version of the AURIC code (Strickland et al., 1999). For a study of Europa's atmosphere of Hall et al. (1995), this algorithm predicts that on average one photon is emitted at OI λ135.6 nm per every 40 ion pairs which are produced by direct excitation of magnetospheric electrons and by secondary electrons ejected following ionization within a pure O_2 atmosphere.

As a consequence of the study of Cunningham et al. (2015), Callisto is expected to be the only Galilean satellite where photoelectrons are the dominant driver of the observed atmospheric UV emission. In contrast to Callisto, the atmospheric UV emission at Io, Europa and Ganymede is predominantly caused by upstreaming magnetospheric electrons of the Jovian magnetosphere or electron acceleration processes in the vicinity of the moon (in case of Ganymede) (Retherford et al., 2000; Roth et al., 2014; Saur et al., 2015; 2000; 1998). Therefore, we cannot adopt physical descriptions of the UV emission process from other Galilean satellites for Callisto.

In this work, we derive a three-dimensional model of the electron energy distribution function in a photoionization driven day side ionosphere which is suited to interpret the observations of Cunningham et al. (2015) and Kliore et al. (2002) simultaneously. The expected energy distribution function of photoelectrons exhibits non-Maxwellian characteristics (e.g., Stamnes and Rees, 1983). Therefore, we utilize a combination of fluid approach and kinetic approach.

In the context of Earth's ionosphere, descriptions of ionospheric photoelectron populations have been intensively discussed in the 1970s (e.g., Banks and Kockarts, 1973). Some of these descriptions focus on the local energy degradation of electrons, while electron transport is neglected or approximated (e.g., Ashihara and Takayanagi, 1974; Jasperse, 1976; 1977). Moreover, local energy degradation has been also considered together with electron transport, for example, within the two-stream method (e.g., Banks and Kockarts, 1973).

We use a kinetic electron energy degradation scheme for suprathermal electrons coupled with a fluid description of the thermal electrons and ions (e.g., Stamnes and Rees, 1983). Similar to Ashihara and Takayanagi (1974), we neglect the effect of transport but consider the energetically important local processes. Our model yields electron energy distribution functions at every location within a prescribed static atmosphere. From these distribution functions we derive the spatial distribution of the two observables: electron density and atmospheric UV emission intensity. The prescribed neutral atmosphere is varied in density and structure within a physical framework in order to find the best fit to individual observations of Kliore et al. (2002) and Cunningham et al. (2015).

An important question about Callisto's atmosphere is what are the physical processes that maintain it. Liang et al. (2005) developed an one dimensional photochemical model of Callisto's atmosphere indicating that O_2, CO_2 and also H_2O are the most abundant species. Substantial parts of Callisto's surface are covered by water ice and therefore sublimation can produce gaseous H_2O. The O_2 molecule can either be produced by photochemical transformation of these H_2O molecules (Yung and McElroy, 1977) or by sputtering of water ice induced by impinging energetic particles (Johnson, 1990). There are several possible sources of

the CO_2 atmosphere such as sputtering, cometary delivery, impact production or indirect sublimation as CO_2 appears to be trapped in the water ice (McGrath et al., 2004). However, the most dominant process concerning CO_2 has not been identified yet.

We prescribe Callisto's atmosphere under the assumption that O_2 is the dominant atmospheric species as also assumed by Kliore et al. (2002), Liang et al. (2005), Cunningham et al. (2015) and Liuzzo et al. (2015). Therefore, the O_2 part is varied in density and shape rather than CO_2 and H_2O in order to fit the model results to observations. The CO_2 part is assumed to be spherically symmetric with a column density of $0.80^{+0.48}_{-0.48} \times 10^{19}$ m^{-2} in agreement with the measurements reported by Carlson (1999). The H_2O part is assumed to be directly related to the water vapor pressure equilibrium above water ice and, therefore, the H_2O density is a function of the surface temperature distribution. As a result, the spatial atmospheric H_2O density distribution is very asymmetric with a maximum at the subsolar point and a minimum at midnight.

The following sections of this paper are structured as follows: In Section 2, we explain our ionosphere model and its underlying assumptions and the set of ionosphere model equations. In Section 3, we discuss the prescribed atmosphere model in detail. Section 4 includes the presentation of model results, namely calculated electron energy distribution functions, electron densities and UV emission intensities and comparisons of model results with corresponding Galileo and HST/COS observations. In Section 5, we estimate the effects of model simplifications, discuss the limits of our model and consider a possible orbital phase dependency of Callisto's atmosphere ionosphere system, before ending with the major conclusions in Section 6.

2. Description of the ionosphere model

In this section, we explain the major model assumptions, present the model equations and show how we calculate the observables electron density and UV emission intensity.

2.1. Model assumptions

Our model of Callisto's ionosphere is based on three major assumptions:

1. At low altitudes, local collisions between electrons, ions and neutrals dominate over transport processes of electrons, since collision time scales are shorter than transport time scales at altitudes below ~ 45 km (see Section 5.1).
2. Photoionization is the main source of Callisto's ionosphere at the day side and also in the terminator region (e.g., Cunningham et al., 2015).
3. Molecular oxygen (O_2), carbon dioxide (CO_2) and water molecules (H_2O) are the major constituents of Callisto's neutral atmosphere (Carlson, 1999; Cunningham et al., 2015; Kliore et al., 2002; Liang et al., 2005).

According to assumption 3, our model includes three neutral species ($N_n = 3$) with the following nomenclature for the index $s \in [1, N_n]$: $s = 1 \rightarrow O_2$, $s = 2 \rightarrow CO_2$ and $s = 3 \rightarrow H_2O$. O_2^+ ions are the dominant ion population within Callisto's atmosphere as shown by Liang et al. (2005), since it has the lowest ionization energy threshold. Ion chemistry evolves on sufficiently short time scales that the original CO_2^+ and H_2O^+ react with neutrals to form O_2^+ and thus we can assume that all ions interact with electrons as O_2^+ ions (Liang et al., 2005). A comparison of chemical, diffusion and recombination time scales for CO_2^+ and H_2O^+ is given in Appendix A validating this assumption for the major part of the atmosphere. As an exception, H_3O^+ is likely the dominant ion species close to the subsolar point due to the expected large H_2O abundance at this location. However, neglecting this effect does not significantly affect our results as we will later discuss in Section 3.3. Coulomb collisions between electrons dominate over other electron collision processes in the low electron energy regime driving the electron distribution towards a Maxwellian distribution at electron energies below a few eV (e.g., Ashihara and Takayanagi, 1974). Therefore, we subdivide the total photoelectron population into thermal and suprathermal electrons as it has been done by several authors for other photoionization driven planetary ionospheres (e.g., Chen and Nagy, 1978; Stamnes and Rees, 1983). Thermal electrons are treated as a fluid while suprathermal electrons are described kinetically. The transition energy E_t between thermal and suprathermal electrons is defined as the energy value where the thermal (Maxwellian) distribution function and the suprathermal (non-Maxwellian) distribution function have equal intensity (e.g., Stamnes and Rees, 1983).

Since we apply the local approximation, the angular electron distribution is not required and the electron distribution function can be taken as isotropic similar to previous descriptions (e.g., Ashihara and Takayanagi, 1974) (see also Section 5.1). Therefore, we investigate the electron energy distribution function F, which is a function of the position vector $\boldsymbol{r}$ and the electron energy E: $F = F(\boldsymbol{r}, E)$ in units of m^{-3} eV^{-1}.

2.2. Model equations

The model equation for suprathermal electrons is given by the transport-free Boltzmann equation

$$0 = \left(\frac{\delta F}{\delta t}\right)_{\text{local}} = \left(\frac{\delta F}{\delta t}\right)^{en}_{in} + \left(\frac{\delta F}{\delta t}\right)^{ei}_{in} + \left(\frac{\delta F}{\delta t}\right)^{ee}_{el} + \left(\frac{\delta F}{\delta t}\right)^{e}_{prod} + \left(\frac{\delta F}{\delta t}\right)^{en}_{sec}, \quad (1)$$

which contains only local source and loss terms describing collisions or initial production. On the right hand side of Eq. (1) (second row), these changes of the electron energy distribution function are subdivided into collision terms for inelastic electron neutral collisions $(\delta F/\delta t)^{en}_{in}$, inelastic electron ion collisions $(\delta F/\delta t)^{ei}_{in}$ and elastic electron electron collisions $(\delta F/\delta t)^{ee}_{el}$. Additionally, we consider the primary electron production term $(\delta F/\delta t)^{e}_{prod}$ and the secondary electron production term $(\delta F/\delta t)^{en}_{\text{sec}}$.

Due to the large mass difference of electrons in comparison to ions and neutrals, electrons lose only a negligible amount of energy during elastic collisions with neutrals and ions (Rees, 1989). These collisions play an important role regarding the angular distribution of electrons when electron transport is taken into account. Since we neglect electron transport we can also neglect elastic electron neutral collisions and elastic electron ion collisions, when balancing the electron energy budget.

Thermal electrons are characterized by the macroscopic variables electron density n_e and electron temperature T_e, which are described by the continuity equation

$$0 = P^{th}_{pri} + P^{th}_{sec} + P^{th}_{deg} - \alpha(T_e) n_e n_{i,1} \quad (2)$$

and the energy equation

$$0 = Q^{th}_{pri}(T_e) + Q^{th}_{sec}(T_e) + Q^{th}_{deg}(T_e) + Q_{ee}(n_e, T_e) - \sum_s \mathbb{L}^{rot}_s(n_e, T_e) - \sum_s \mathbb{L}^{vib}_s(n_e, T_e) - \alpha(T_e) n_e n_{i,1} \frac{3}{2} k_b T_e, \quad (3)$$

where P^{th}_{pri} is the initial production rate of photoelectrons with energies below the transition energy E_t, P^{th}_{sec} the production rate of secondary electrons with energies below E_t, P^{th}_{deg} the degradation rate which is the thermalization rate of suprathermal electrons due to electron neutral collisions and electron electron collisions, α

the recombination rate coefficient, $n_{i,1}$ the O_2^+ ion density, Q_{pri}^{th} the heating rate due to initial photoelectron production below E_t, Q_{sec}^{th} the heating rate due to secondary electron production below E_t, Q_{deg}^{th} the heating rate due to degradation of electrons from energies above E_t to energies below E_t due to inelastic electron neutral collisions, Q_{ee} the heating rate due to energy transfer from suprathermal electrons to thermal electrons via Coulomb collisions, $\mathbb{L}_s^{rot}$ and $\mathbb{L}_s^{vib}$ the cooling rates due to rotational and vibrational state excitation of neutrals and k_B is the Boltzmann constant. Heat conduction is neglected, as the associated electron energy transport is expected to play a minor role at low altitudes ($\lesssim$ 45 km) similar to our estimates of electron transport at these low altitudes.

The ion density is constrained by mass conservation through

$$0 = P_{pri}^{ion} + P_{sec}^{ion} - \alpha(T_e) n_e n_{i,1}, \tag{4}$$

where P_{pri}^{ion} is the photoionization rate and P_{sec}^{ion} is the ion production rate due to secondary ionization. For our purpose we do not need to consider the conservation of ion energy and calculate the ion temperature, as electron ion collisions are only important in recombination where rates are a weak function of ion temperature.

Finally, we also ensure quasi neutrality of the ionospheric plasma

$$n_e \approx n_{i,1} (= n_{O2+}), \tag{5}$$

where we also use the assumption that O_2^+ is the dominant ion species.

The full set of model equations is given by the coupled Eqs. (1)–(5). In the following we discuss the appearing terms in more detail. Solutions of the above model equations are found numerically as described in Appendix B yielding calculated suprathermal electron energy distribution functions, thermal electron densities and electron temperatures.

2.2.1. Collision terms of suprathermal electrons

According to assumption 2, the primary production term of electrons is given by the energy dependent photoelectron production rate: $(\delta F/\delta t)^e_{prod} = \sum_s P_{e,s}$. For a given neutral species s, Rees (1989) gives the following expression of this production rate in m^{-3} s^{-1} eV^{-1}:

$$P_{e,s}(\boldsymbol{r}, E) = n_{n,s}(\boldsymbol{r}) \sum_l \int \mathrm{d}\lambda \; I^{\infty}(\lambda) \; e^{-\tau(\boldsymbol{r},\lambda)} \times \sigma_s^i(\lambda) \; p_{sl}(\lambda) \; \delta\big(E - E'_{sl}(\lambda)\big), \tag{6}$$

where $n_{n,s}(\boldsymbol{r})$ is the neutral particle's number density in m^{-3} at the location $\boldsymbol{r}$, l the index denoting possible ion states, λ the wavelength of the incoming photon in nm, I^{∞} the solar photon flux as a function of wavelength at the top of Callisto's atmosphere in m^{-2} s^{-1} nm^{-1}, τ the optical depth, σ_s^i the photoionization cross section in m^2, p_{sl} the branching ratio of the final ion state l and E'_{sl} represents the initial photon energy minus the ionization threshold energy (e.g., Rees, 1989):

$$E'_{sl}(\lambda) = hc\left(\frac{1}{\lambda} - \frac{1}{\lambda^0_{sl}}\right), \tag{7}$$

where λ^0_{sl} is the threshold ionization wavelength of the ion state l in nm, h is the Planck constant in eV s and c the speed of light in nm s^{-1}. In Eq. (6), the delta function $\delta\big(E - E'_{sl}(\lambda)\big)$ with the unit eV^{-1} ensures that the energy of a produced photoelectron is equal to E'_{sl}. The optical depth $\tau(\boldsymbol{r}, \lambda)$ is given by (e.g., Rees, 1989)

$$\tau(\boldsymbol{r}, \lambda) = \sum_s \sigma_s^a(\lambda) \int_{\boldsymbol{\Gamma_r}} n_{n,s}(\boldsymbol{r}') \; \mathrm{d}\boldsymbol{r}', \tag{8}$$

where σ_s^a is the photon absorption cross section of the neutral species s in m^2 and $\boldsymbol{\Gamma_r}$ represents the ray path along the direction to the Sun between location $\boldsymbol{r}$ and the top of Callisto's atmosphere. For Eq. (8), the integration is conducted numerically delivering optical depths for all subsolar angles (i.e., solar zenith angles).

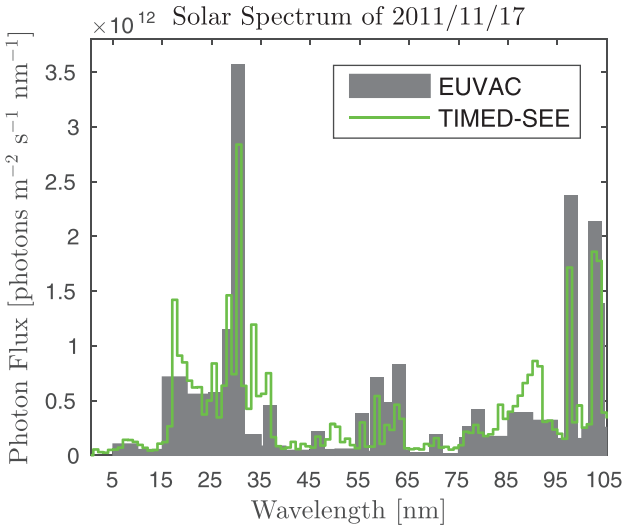

Fig. 1. Solar photon fluxes at Callisto's solar distance on the 17th of November, 2011. The green line marks the solar photon fluxes obtained by using the TIMED-SEE data and the gray bars mark the solar photon fluxes obtained from the EUVAC model. (For interpretation of the references to colour in this figure legend, the reader is referred to the web version of this article.)

Photoionization and photon absorption cross sections σ_s^i and σ_s^a of all species are taken from Schunk and Nagy (2009). Branching ratios p_{1l} and threshold wavelengths λ^0_{1l} of O_2 are taken from Rees (1989), branching ratios p_{2l} and threshold wavelengths λ^0_{2l} of CO_2 are taken from Schunk and Nagy (2009) and Itikawa (2002) and branching ratios p_{3l} and threshold wavelengths λ^0_{3l} of H_2O are taken from Schunk and Nagy (2009) and Itikawa (2005). In summary, the set of expressions (6)–(8) determines the photoelectron production term $(\delta F/\delta t)^e_{prod}$.

The solar photon flux I^{∞} is the only external time variable parameter of the photoelectron production term. This time variable flux is implemented through the EUVAC model of Richards et al. (1994) covering a photon wavelength range of 5–105 nm. Since 2003, the 'Solar EUV Experiment' (SEE) on-board the 'Thermosphere Ionosphere Mesosphere Energetics and Dynamics' (TIMED) mission spacecraft measures the solar photon flux directly at 1 AU providing a better resolution than the EUVAC model and a smaller cutoff wavelength of 0.5 nm. However, as we simulate configurations of Galileo flybys from before 2003 (C-9, C-20, C-22, C-23) we use EUVAC fluxes for our model.

Fig. 1 shows a comparison of EUVAC fluxes (gray bars) with TIMED-SEE fluxes (green line) at Callisto's solar distance for the 17th of November 2011, the date of the HST/COS observation of Callisto's UV emission reported in Cunningham et al. (2015). This comparison shows that the EUVAC fluxes and the TIMED-SEE fluxes do not significantly differ at this specific day except that the TIMED-SEE flux distribution exhibits naturally more fine structures and also covers the wavelength range of 0.5-5 nm.

Due to this lower cutoff wavelength, the TIMED-SEE photon flux includes also most of the soft x-ray radiation, which ranges from 0.1 to 7 nm. At Callisto, soft x-ray radiation plays only a minor role in the ionosphere formation. According to the observations of Carlson (1999) and Cunningham et al. (2015) we expect Callisto's atmosphere to be optically thin and to be composed of O_2, CO_2 and H_2O. For such an atmosphere, we calculate electron production rates using the TIMED-SEE fluxes showing that less than 1% of the total photoelectron production and less than 3% of

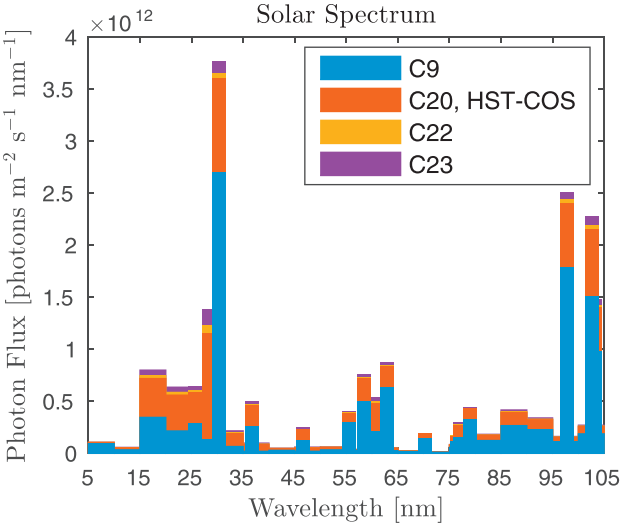

Fig. 2. EUVAC solar photon fluxes at Callisto's solar distance for C-9, C-20, C-22, C-23 and the HST/COS observation. The fluxes are plotted overlapping. The largest fluxes occurred during C-23 while the smallest fluxes occurred during C-9. The according dates are: C-9: 1997/06/25, C-20: 1999/05/05, C-22: 1999/08/14, C-23: 1999/09/16, HST/COS: 2011/11/17.

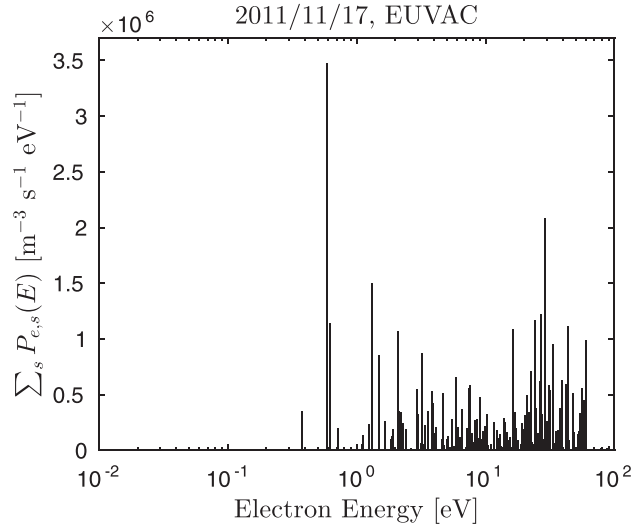

Fig. 3. Photoelectron production rate $\Sigma_s P_{e,s}$ as a function of photoelectron energy (photoelectron spectrum) of an exemplary volume element at Callisto's solar distance with O_2 density $n_{n,1} = 1.0 \times 10^{15}$ m^{-3}, CO_2 density $n_{n,2} = 0.25 \times 10^{15}$ m^{-3} and H_2O density $n_{n,3} = 1.0 \times 10^{15}$ m^{-3}. These rates are calculated by using the EUVAC solar photon fluxes of the 17th of November, 2011, shown in Fig. 1.

the total photoelectron energy production is caused by photons with wavelengths smaller than 5 nm, which are not included in the EUVAC model. As our model works with TIMED-SEE fluxes and EUVAC fluxes as well, we find that our model results are not significantly affected by the choice of the flux type and the lower cutoff wavelength regarding the date of the 17th of November 2011. Therefore, we come to the conclusion that the EUVAC model sufficiently describes the ionizing solar radiation for the purpose of our aeronomic calculations regarding Callisto.

Fig. 2 shows EUVAC solar photon fluxes according to the times of flybys C-9, C-20, C-22 and C-23 and the HST/COS observation of the 17th of November 2011. EUVAC fluxes during C-20, C-22, C-23 and the HST/COS observation are quite similar, in fact, EUVAC fluxes during C-20 and the HST/COS observation are nearly indistinguishable. During C-9 the EUVAC model predicts solar fluxes that are on average $\sim$ 35% lower than during the other observations.

Based on the EUVAC fluxes of the 17th of November 2011, Fig. 3 shows the calculated discretized photoelectron spectrum of an exemplary atmospheric volume element. Photoelectrons are produced non-uniformly in energy space between 0.3 and $\sim$ 100 eV. Only a negligible amount of electrons ($<$ 1%) and electron energy ($<$ 3%) is produced above 100 eV. There is a strong peak at 0.6 eV, which results from the 97.702 nm CIII resonance peak of the solar photon flux spectrum (see also Fig. 1). This photoelectron production peak is very distinct since only the lowest ion states of O_2^+ and H_2O^+ with threshold energies of 12.1 and 12.64 eV can get excited by photons with a wavelength of 97.702 nm corresponding to an energy of 12.7 eV. A second more diffuse peak is located around 25 eV, which is caused by the prominent 30.331 nm HeII resonance peak of the solar spectrum. The associated photons with energies of 40.8 eV can excite several different ion states causing the diffuse peak characteristic. Note that photoelectrons with energies larger than $\sim$ 14 eV cause dissociative excitation of O_2, which is the underlying process of the atmospheric OI λ135.6 and OI λ130.4 nm emissions.

After the description of the primary electron production term we focus on the remaining collision terms in Eq. (1). Our model contains the energetically important inelastic collisions of electrons with O_2, CO_2, H_2O including secondary ionization, dissociative recombination with O_2^+ ions as well as electron electron collisions.

For a given neutral species s, an electron neutral collision process of type t_s is characterized by its species-specific energy-dependent cross section $\sigma_{st_s}(E)$ and the associated discrete electron energy loss ϵ_{st_s}, where t_s counts all possible collision processes up to the total amount of processes T_s. The set of electron collisions with O_2 includes electron impact ionization, electron impact dissociation, excitation of the electronic states $a^1\Delta$, $b^1\Sigma$, 3Π, ACc, Schumann-Runge continuum (SR) and unidentified states (uid), excitation of the rotational state J 1–3 and excitation of the vibrational states $\nu' = 1, 2, 3, 4$ excited from the ground state $\nu' = 0$. The set of electron collisions with CO_2 includes electron impact ionization, excitation of the electronic states $^1\Sigma_u^+$ and $^1\Pi_u$, excitation of the rotational state J 0–2 and excitation of the vibrational states (100), (010), and (001), excited from the ground state (000). The set of electron collisions with H_2O includes electron impact ionization, excitation of the electronic state $3B_1$, excitation of the rotational state J 0–1 and excitation of the vibrational states (100), (010) and (001), excited from the ground state (000). Table 1 shows all considered electron neutral collision processes together with the used discrete energy loss values and references for the associated cross section data.

In order to incorporate electron production due to secondary electron impact ionization, we use the expression for the normalized electron impact ionization double cross section $\sigma_{I,s}(E_p, E'_{new})$ of Opal et al. (1971), scaled with recent total ionization cross section data of O_2, CO_2 and H_2O presented by Anzai et al. (2012). In the context of secondary electron impact ionization, E_p is the energy of the primary electron before the collision, E'_{new} is the energy of the newly produced secondary electron (after the collision) and I_s is the electron impact ionization threshold energy. Since the amount of kinetic energy transferred to the newly created ion can be neglected these energies are related to each other by $E'_{new} = E_p - I_s$ (Opal et al., 1971).

We approximate the discrete energy loss of electron impact ionization by the energy of the newly created electron plus the ionization threshold energy needed to produce the ion ground state, which is the most probable final ion state for O_2, CO_2 and H_2O within the investigated electron energy range. Nevertheless

Table 1
List of inelastic electron neutral collisions and associated discrete energy losses. *Energy loss of rotational excitation of O_2, CO_2 and H_2O is implemented in the model according to the method of Swartz (1985) with cross sections rescaled by a factor of 0.2, 0.02 and 0.4, respectively, real energy losses are 2.0×10^{-3} eV for O_2, 2.0×10^{-4} eV for CO_2 and 4.0×10^{-3} eV for H_2O.

Physical process	Energy loss	Cross section reference
O_2	ϵ_{1,t_1}	
Rotational excitation J 1–3	*0.01 eV	Itikawa (2009)
Vibrational excitation $v = 0 - 1$	0.29 eV	Allan (1995)
Vibrational excitation $v = 0 - 2$	0.49 eV	Allan (1995)
Vibrational excitation $v = 0 - 3$	0.68 eV	Allan (1995)
Vibrational excitation $v = 0 - 4$	0.87 eV	Allan (1995)
Electronic excitation $a^1\Delta$	0.98 eV	Itikawa (2009)
Electronic excitation $b^1\Sigma$	1.63 eV	Itikawa (2009)
Electronic excitation ACc	4.20 eV	Itikawa (2009)
Dissociation	5.12 eV	Anzai et al. (2012)
Electronic excitation SR	7.10 eV	Itikawa (2009)
Electronic excitation 3Π	8.10 eV	Itikawa (2009)
Electronic excitation uid	8.90 eV	Itikawa (2009)
Ionization	12.10 eV	Hwang et al. (1996)
Dissociative excitation 135.6 nm	14.26 eV	Kanik et al. (2003)
Dissociative excitation 130.4 nm	14.62 eV	Kanik et al. (2003)
CO_2	ϵ_{2,t_2}	
Rotational excitation J 0–2	*0.01 eV	Takayanagi and Itikawa (1970)
Vibrational excitation (010)	0.06 eV	Itikawa (2002)
Vibrational excitation (100)	0.16 eV	Itikawa (2002)
Vibrational excitation (001)	0.18 eV	Itikawa (2002)
Electronic excitation Σ_u^+	11.00 eV	Itikawa (2002)
Electronic excitation $^1\Pi_u$	11.39 eV	Itikawa (2002)
Ionization	13.80 eV	Itikawa (2002)
H_2O	ϵ_{3,t_3}	
Rotational excitation J 0–1	*0.01 eV	Itikawa (2005)
Vibrational excitation (010)	0.20 eV	Itikawa (2005)
Vibrational excitation (100) + (001)	0.46 eV	Itikawa (2005)
Electronic excitation $3B_1$	10.40 eV	Anzai et al. (2012)
Ionization	12.62 eV	Itikawa (2005)

we use total ionization cross sections which include also ionizations of higher order ion states. However, since we neglect the additional energy loss from excitations of higher order ion states, the energy loss by electron impact ionization is underestimated by approximately 15%. This error has been estimated by comparing the applied energy loss to an average energy loss, which is calculated by averaging the threshold energies of all ion excitation states weighted by the associated excitation probabilities.

Summing up all mentioned processes, the inelastic electron neutral collision term is then given by (e.g., Ashihara and Takayanagi, 1974)

$$\begin{aligned}\left(\frac{\delta F}{\delta t}\right)_{in}^{en} = & \sqrt{\frac{2}{m_e}} \sum_s^{N_n} n_{n,s} \int_{I_s}^{E_{max}} d\tilde{E}\ \sqrt{E+\tilde{E}} \\ & \times \sigma_{I,s}(E+\tilde{E}, \tilde{E}-I_s)\ F(E+\tilde{E}) \\ & + \sqrt{\frac{2}{m_e}} \sum_s^{N_n} n_{n,s} \sum_{t_s=1}^{T_s-1} \sqrt{E+\epsilon_{st_s}}\ \sigma_{st_s}(E+\epsilon_{st_s}) F(E+\epsilon_{st_s}) \\ & - \sqrt{\frac{2}{m_e}} \sum_s^{N_n} n_{n,s} \sum_{t_s=1}^{T_s} \sqrt{E}\ \sigma_{st_s}(E) F(E), \end{aligned} \quad (9)$$

where the first term on the right hand side represents the source of electrons of energy E due to degradation of electrons after ionizing collisions. The second term represents the electron source due to degradation of electrons after non-ionizing collisions and the third term represents the loss due to energy degradation of electrons of energy E. The electron neutral collision marked by index $t_s = T_s$ is the electron impact ionization process and E_{max} denotes the maximum energy above which no photoelectron is produced. The production of secondary electrons from ionizing electron neutral collisions is implemented through (e.g., Ashihara and Takayanagi, 1974)

$$\begin{aligned}\left(\frac{\delta F}{\delta t}\right)_{sec}^{en} = & \sqrt{\frac{2}{m_e}} \sum_s^{N_n} n_{n,s} \int_{I_s}^{E_{max}} d\tilde{E}\ \sqrt{E+\tilde{E}} \\ & \times \sigma_{I,s}(E+\tilde{E}, E)\ F(E+\tilde{E}). \end{aligned} \quad (10)$$

The most important inelastic electron ion collision is dissociative recombination of electrons with O_2^+ as it dominates over other electron ion processes below collision energies of 15 eV (Sheehan and St Maurice, 2004). Dissociative recombination cross sections of O_2^+ $\sigma_{rec,1}$ are given by Peverall et al. (2001) up to collision energies of 3 eV. For our purpose, recombination can be neglected above this data limit of 3 eV, since collision rates of inelastic electron neutral collisions and elastic electron electron collisions are much larger than recombination rates for energies larger than 3 eV. For a given O_2^+ ion density $n_{i,1}$, the associated recombination collision term is given by (e.g., Ashihara and Takayanagi, 1974)

$$\left(\frac{\delta F}{\delta t}\right)_{in}^{ei} = -\sqrt{\frac{2}{m_e}}\ n_{i,1}\ \sqrt{E}\ \sigma_{rec,1}(E)\ F(E). \quad (11)$$

Energy is exchanged between electrons via Coulomb collisions. In contrast to the discrete energy loss from collisions with neutrals, suprathermal electrons lose energy continuously by Coulomb collisions with thermal electrons. In order to describe this process for suprathermal electrons, we use the effective electron electron collision cross section $\sigma_{ee}(E, n_e, T_e)$ introduced by Nagy and Banks (1970), which is a function of suprathermal electron energy, thermal electron density and temperature. This cross section

is given by

$$\sigma_{ee}(E, n_e, T_e) = \frac{1}{\Delta E}\frac{1}{n_e}\left(\frac{dE}{dx}\right), \tag{12}$$

where ΔE is the discretized energy loss that is set to the numerical energy bin width, $(1/n_e)(dE/dx)$ is the suprathermal electron energy loss rate per unit length in m^2 eV. Swartz et al. (1971) give the following approximative analytic expression for this loss rate based on fitting the results of Butler and Buckingham (1962):

$$\frac{1}{n_e}\left(\frac{dE}{dx}\right) \approx \frac{5.10\times10^{-12}}{E^{0.94}n_e^{0.03}}\left(\frac{E-E_0}{E-0.53\ E_0}\right)^{2.36} \tag{13}$$

with $E_0 = 8.617\times10^{-5}T_e$, temperatures in K, densities in m^{-3} and energies in eV. Thus, the applicable electron electron collision term is given by

$$\left(\frac{\delta F}{\delta t}\right)_{ee}^{el} = \sqrt{\frac{2}{m_e}}\ n_e\ \sqrt{E+\Delta E}\ \sigma_{ee}(E+\Delta E, n_e, T_e)\ F(E+\Delta E) - \sqrt{\frac{2}{m_e}}\ n_e\ \sqrt{E}\ \sigma_{ee}(E, n_e, T_e)\ F(E). \tag{14}$$

2.2.2. Sources and sinks of thermal electrons and thermal electron energy

Thermal electrons are produced by (a) initial photoionization producing electrons with energies smaller than the transition energy, (b) secondary ionization and (c) degradation of suprathermal electrons down below the transition energy. The corresponding production terms listed in Eq. (2) are given by:

$$\text{(a)}\ P_{pri}^{th} = \sum_s \int_0^{E_t} P_{e,s}(E)\ dE, \tag{15}$$

$$\text{(b)}\ P_{sec}^{th} = \int_0^{E_t}\left(\frac{\delta F}{\delta t}\right)_{en}^{sec} dE, \tag{16}$$

$$\text{(c)}\ P_{deg}^{th} = -\int_{E_t}^{E_{max}}\left[\left(\frac{\delta F}{\delta t}\right)_{en}^{in} + \left(\frac{\delta F}{\delta t}\right)_{el}^{ee}\right] dE. \tag{17}$$

The associated heating rates listed in Eq. (3) are accordingly given by:

$$\text{(a)}\ Q_{pri}^{th}(T_e) = \sum_s \int_0^{E_t} P_{e,s}(E)\left(E-\frac{3}{2}k_BT_e\right) dE, \tag{18}$$

$$\text{(b)}\ Q_{sec}^{th}(T_e) = \int_0^{E_t}\left(\frac{\delta F}{\delta t}\right)_{en}^{sec}\left(E-\frac{3}{2}k_BT_e\right) dE, \tag{19}$$

$$\text{(c)}\ Q_{deg}^{th}(T_e) = \sqrt{\frac{2}{m_e}}\sum_s^{N_n} n_{n,s}\sum_{t_s}^{T_s}\int_{E_t}^{E_t+\epsilon_{s,t_s}}\sqrt{E} \times \sigma_{st_s}(E)\ F(E)\left(E-\epsilon_{st_s}-\frac{3}{2}k_BT_e\right)dE. \tag{20}$$

The heating rate Q_{deg}^{th} includes only the heating due to discrete degradation through electron neutral collisions, electron electron collisions are treated separately. Heating rates (a)–(c) are minor in comparison to the heating rate Q_{ee} that is generated by electron electron collisions (Schunk and Nagy, 1978). Since electron electron collisions only redistribute energy within the electron population, the heating rate of thermal electron is given by the negative integrated cooling rate of suprathermal electrons (Hoegy, 1984):

$$Q_{ee}(n_e, T_e) = -\int_{E_t}^{E_{max}}\left(\frac{dF}{dt}\right)_{ee}\left(E-\frac{3}{2}k_BT_e\right) dE = \sqrt{\frac{2}{m_e}}\ \sqrt{E_t}\ F(E_t)\left(\frac{dE}{dx}\right)(E_t-\frac{3}{2}k_BT_e) + \sqrt{\frac{2}{m_e}}\int_{E_t+\Delta E}^{E_{max}}\sqrt{E}\ F(E)\left(\frac{dE}{dx}\right)dE \tag{21}$$

Within our model, the only loss process of thermal electrons is dissociative recombination with the major ion O_2^+. The corresponding reaction coefficient is given by Sheehan and St Maurice (2004) as a function of electron temperature:

$$\alpha(T_e) = 1.95\times10^{-13}\ m^3s^{-1}\left(\frac{T_e}{300\ K}\right)^h, \tag{22}$$

$$h = \begin{cases} -0.70 & \text{, if } T_e \le 1200\ K \\ -0.56 & \text{, if } T_e > 1200\ K. \end{cases} \tag{23}$$

The corresponding loss of energy is implemented through $\alpha(T_e)\,n_e\,n_{i,1}\,(3/2\,k_bT_e)$.

Inelastic electron neutral collisions leading to excitation of rotational and vibrational states play an important role regarding energy loss of thermal electrons. Analytic expressions for cooling rates generated by rotational state excitation of O_2, CO_2 (Dalgarno, 1969) and H_2O (Cravens and Korosmezey, 1986) are given in units of eV m^{-3} s^{-1}:

$$O_2:\quad \mathbb{L}_1^{rot}(n_e, T_e) = 6.9\times10^{-20}\ n_e\ n_{n,1}\ \frac{T_e-T_n}{T_e^{1/2}}, \tag{24}$$

$$CO_2:\quad \mathbb{L}_2^{rot}(n_e, T_e) = 5.8\times10^{-20}\ n_e\ n_{n,2}\ \frac{T_e-T_n}{T_e^{1/2}}, \tag{25}$$

$$H_2O:\quad \mathbb{L}_3^{rot}(n_e, T_e) = n_e\ n_{n,3}\left(a+b\ \ln\left(\frac{T_e}{T_n}\right)\right)\left(\frac{T_e-T_n}{T_e^{5/4}}\right), \tag{26}$$

$$a = 1.052\times10^{-14} + 6.043\times10^{-16}\ \ln(T_n), \tag{27}$$

$$b = 4.180\times10^{-15} + 2.026\times10^{-16}\ \ln(T_n), \tag{28}$$

where all densities are in m^{-3}, temperatures are in K and T_n is the temperature of the neutrals which is approximated by 120 K corresponding to the average surface temperature of Callisto's day side hemisphere (Hanel et al., 1979). For rotational state excitation of neutrals, the neutral temperature needs to be taken into account since electrons with energies comparable to the energies of the neutral particles can still excite rotational states.

Vibrational state excitation thresholds are at least one order of magnitude larger than rotational state excitation thresholds. Therefore, we neglect the neutral temperature dependency of vibrational cooling. For each neutral species s, these cooling rates are then given by

$$\mathbb{L}_s^{vib}(n_e, T_e) = n_e\ n_{n,s}\sqrt{\frac{1}{\pi m_e}}\left(\frac{2}{k_BT_e}\right)^{3/2}\sum_m E_{s,m}^{vib} \times \int_0^{E_{max}} E\ \sigma_{s,m}^{vib}(E)\ e^{-\frac{E}{k_BT_e}}\ dE, \tag{29}$$

where the sum is taken over different vibrational excitation states m which are the same as for suprathermal electrons (see Table 1). Vibrational state excitation cross sections $\sigma_{s,m}^{vib}$ (in m^2) and vibrational state excitation energies $E_{s,m}^{vib}$ (in eV) are taken from Allan (1995) and Itikawa (2009) for O_2, from Itikawa (2002) for CO_2 and from Itikawa (2005) for H_2O.

2.2.3. Sources and sinks of ions

Primary and secondary ion production rates are given by

$$P_{pri}^{ion} = \sum_{s}^{N_n} \int_0^{E_{max}} P_{e,s}(E)\ dE, \tag{30}$$

$$P_{sec}^{ion} = \sqrt{\frac{2}{m_e}} \sum_{s}^{N_n} n_{n,s} \int_{E_t}^{E_{max}} \sqrt{E}\ \sigma_{sT_s}(E) F(E)\ \mathrm{d}E, \tag{31}$$

with $\sigma_{sT_s}(E) = \int_0^{\infty} \sigma_{I,s}(E, E')\ \mathrm{d}E'$. Ions get lost in the same way as electrons due to dissociative recombination as described by Eq. (4).

2.3. Extracting observables: electron density and ultraviolet emission

In the following section we describe how we extract the observables electron density and UV emission intensity from the solution of our model equations for comparison with the observations of Kliore et al. (2002) and Cunningham et al. (2015).

2.3.1. Electron densities

Kliore et al. (2002) published electron density altitude profiles of radio occultation entry and exit observations of Galileo flybys C-9, C-20, C-22 and C-23. These profiles were calculated under the assumption of a spherically symmetric ionosphere. We cannot directly compare electron density altitude profiles of Kliore et al. (2002) with our model results, since our photoionization driven model yields strong day night asymmetries of the ionosphere. Therefore, we calculate the electron column densities along the radio occultation line of sight (LOS) N_{LOS}^{e} using both our model and results of Kliore et al. (2002):

$$N_{\mathrm{LOS}}^{e}(\boldsymbol{r}_t, z_{int}) = \int_{\boldsymbol{\Gamma}^{\mathrm{LOS}}(\boldsymbol{r}_t, z_{int})} n_e(\boldsymbol{r}')\ \mathrm{d}\boldsymbol{r}', \tag{32}$$

with $\boldsymbol{\Gamma}^{\mathrm{LOS}}(\boldsymbol{r}_t, z_{int})$ representing the path of the LOS as a function of latitude and longitude ($\boldsymbol{r}_t$) where the LOS is tangential and thus closest to Callisto's surface and the altitude of the closest approach of the LOS z_{int}. The LOS electron column density N_{LOS}^{e} allows a direct comparison between observation and model. Fig. 4 illustrates how we determine the quantity N_{LOS}^{e} for both model and observation. All panels of Fig. 4 show electron densities in the equatorial plane with focus on the terminator regions. Both left panels show a spherically symmetric ionosphere that is extracted from the radio occultation data (Kliore et al., 2002, Figure 2) of C-22 entry (upper left panel) and exit (lower left panel). The right panels of Fig. 4 show a day night asymmetric ionosphere which is a result of our model. All panels also show white lines representing the radio occultation LOSs of four different closest approach altitudes z_{int} (0 km, 25 km, 50 km and 75 km) for C-22 entry (upper panels) and exit (lower panels).

For both the results of Kliore et al. (2002) and the results of our model, we derive the LOS electron column densities by integrating the electron densities along the LOSs that are represented by these white lines. In case of $z_{int} = 0$, the LOS is assumed to be tangential to the surface crossing the tangential point $\boldsymbol{r}_t$. The LOS of integration altitudes larger than zero are assumed to be shifted parallel to the tangential LOS radially outward. The choice of the integration altitudes is based on the altitude profiles from Kliore et al. (2002). Table 2 lists the spherical coordinates of the tangential points $\boldsymbol{r}_t$ of entries and exits of all four flybys according to the west longitude planetographic coordinate system. This geometric information was taken from Fig. 2 of Kliore et al. (2002).

For our model, electron density distributions along radio occultation LOSs are derived from solving the model equations for each volume element along the LOSs. Therefore, we directly calculate the electron energy distribution functions and associated electron densities along equally spaced 1-D grids of radio occultation LOSs, for which we use 600 grid points with a spatial resolution of ~ 8 km. Finer resolutions do not significantly change the model results.

Table 2
Spherical coordinates (ϕ_T, θ_T) of electron altitude profile foot points (tangential points $\boldsymbol{r}_t$) in degree according to west longitude planetographic coordinate system taken from Kliore et al. (2002).

	C-9	C-20	C-22	C-23
Entry ϕ_T	164.3°	352.7°	350.9°	351.6°
Entry θ_T	88.8°	81.4°	86.4°	83.4°
Exit ϕ_T	344.4°	170.8°	172.1°	171.2°
Exit θ_T	87.2°	89.2°	82.5°	86.4°

2.3.2. Ultraviolet emission intensities

From the electron energy distribution functions of all atmospheric volume elements, we calculate the brightness of the disk averaged atmospheric UV emission I_λ in Rayleigh for the OI λ135.6 nm and OI λ130.4 nm multiplets and the HI λ121.6 nm line similar to Saur et al. (1998):

$$I_{130.4} = \frac{10^{-10}}{R_C^2 \pi} \sqrt{\frac{2}{m_e}} \int_{\mathrm{Atm.}} \int_0^{E_{max}} \sqrt{E}\ F(\boldsymbol{r}, E)\ e^{-\tau(\boldsymbol{r}, 130.4\mathrm{nm})} \times [n_{n,1}(\boldsymbol{r})\ \sigma_{130.4,1}(E) + n_{n,3}(\boldsymbol{r})\ \sigma_{130.4,3}(E)]\ \mathrm{d}E\ \mathrm{d}V, \tag{33}$$

$$I_{135.6} = \frac{10^{-10}}{R_C^2 \pi} \sqrt{\frac{2}{m_e}} \int_{\mathrm{Atm.}} \int_0^{E_{max}} \sqrt{E}\ F(\boldsymbol{r}, E)\ e^{-\tau(\boldsymbol{r}, 135.6\mathrm{nm})} \times\ n_{n,1}(\boldsymbol{r})\ \sigma_{135.6,1}(E)\ \mathrm{d}E\ \mathrm{d}V, \tag{34}$$

$$I_{121.6} = \frac{10^{-10}}{R_C^2 \pi} \sqrt{\frac{2}{m_e}} \int_{\mathrm{Atm.}} \int_0^{E_{max}} \sqrt{E}\ F(\boldsymbol{r}, E)\ e^{-\tau(\boldsymbol{r}, 121.6\mathrm{nm})} \times\ n_{n,3}(\boldsymbol{r})\ \sigma_{121.6,3}(E)\ \mathrm{d}E\ \mathrm{d}V. \tag{35}$$

In these expressions, $R_C = 2410$ km is Callisto's radius, $\sigma_{130.4,\,1}$ and $\sigma_{135.6,\,1}$ are the cross sections of electron impact dissociative excitation of O_2 associated with the photon emission at 103.4 and 135.6 nm taken from Kanik et al. (2003) and $\sigma_{121.6,\,3}$ and $\sigma_{130.4,\,3}$ are the cross sections of electron impact dissociative excitation of H_2O associated with the photon emission at 121.6 nm (Lyman-α) and 130.4 nm taken from Makarov et al. (2004). The contribution of H_2O to the OI λ135.6 nm emission line is negligible. We account for atmospheric re-absorption of the UV emission by the term $exp\{-\tau(\boldsymbol{r}, \lambda)\}$ where we have approximated the Callisto-HST line by the Callisto-Sun line (only for the purpose of calculating re-absorption). Re-absorption is expected to weaken Callisto's atmospheric UV emission intensity by ~ 5% (Cunningham et al., 2015). OI emission line cross sections are non-zero for electron energies larger than approximately 14 eV. This threshold shows that the UV emission intensity can only be generated by the high-energy part of the electron energy distribution function (~ 14 eV - 100 eV).

The spatial integration in Eqs. (33)–(35) is conducted numerically using a spherical grid (r_i, θ_j, ϕ_k) with a radial resolution of 6.5 km and an angular resolution of 2°. In order to improve the computational performance, we will reduce the problem to two dimensions if the prescribed neutral atmosphere is symmetric with respect to the Sun-Callisto axis.

3. The prescribed atmosphere

The ionosphere model, described in Section 2, is applied to a prescribed atmosphere which is based on the assumption of three major atmospheric species namely O_2, CO_2 and H_2O. Similar to Liang et al. (2005), we assume exponentially decreasing density

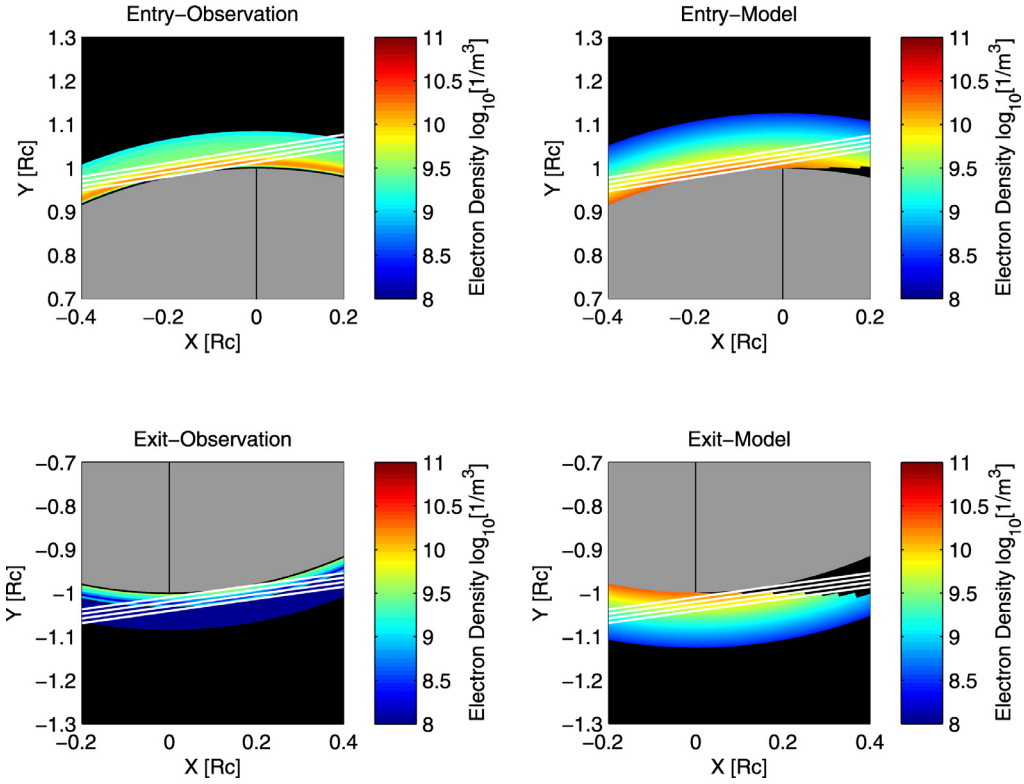

Fig. 4. Electron densities of the terminator regions in the equatorial plane according to the C-22 entry and exit electron density altitude profiles of Kliore et al. (2002) (left panels) and according to an exemplary model ionosphere with configurations of C-22 (right panels). For the shown model results (right panels), the prescribed atmosphere is spherically symmetric with an O_2 column density of 3.0×10^{19} m^{-2}. White lines correspond to radio occultation LOS during entry (upper row) and exit (lower row) of flyby C-22. In this Cartesian coordinate system, the Sun is in the -x direction and the y-axis is in the equatorial plane. Length scales are given in units of Callisto's radius $R_C = 2410$ km.

altitude profiles with a constant scale height H of 30 km for all species. Note that our atmosphere model is a parametrized and phenomenological model. We use our physical ionosphere model in combination with this atmosphere model to find constraints on Callisto's atmosphere that might be interesting for subsequent physical models of Callisto's atmosphere.

3.1. O_2

The prescribed O_2 atmosphere model allows for an independent variation of the subsolar O_2 column density and the terminator O_2 column density due to the following reasons: The O_2 part of Callisto's atmosphere is believed to be created by surface sputtering induced by precipitating magnetospheric ions and by a series of photochemical reactions of sublimated H_2O molecules (Johnson, 1990; Yung and McElroy, 1977). The sputtering yield of O_2 molecules and the sublimation rate decreases with decreasing surface temperature (Famá et al., 2008), which introduces a day night asymmetry of the O_2 production rate. Modeling work on the sputtering dominated O_2 atmosphere of Europa by Plainaki et al. (2013) shows that this asymmetry of the production rate can also cause a day night asymmetry of the atmospheric O_2 column density. They also show that the O_2 column density possibly scales with the orbital phase of Europa as a result of the inhomogeneous sputtering efficiency distribution caused by surface temperature and the inhomogeneous ion precipitation rate. The total O_2 column density maximum occurs at the subsolar point when the direction of the sunlight and the magnetospheric plasma are aligned and the total minimum occurs on the night side during anti-parallel alignment. Results of Plainaki et al. (2013) indicate that the solar illumination is the dominant driver of Europa's atmospheric asymmetry causing a day night asymmetry for all orbital phases. Assuming that surface sputtering plays a major role in creating Callisto's O_2 atmosphere, the O_2 column density of Callisto's atmosphere has probably also a day night asymmetry and might scale with the orbital phase.

To incorporate asymmetric effects, we parametrize the atmospheric O_2 column density N_{O2} in the following way:

$$N_{O2}(\beta) = \begin{cases} \frac{1}{2}\left(N_{O2}^{max} + N_{O2}^{min}\right) + \frac{1}{2}\left(N_{O2}^{max} - N_{O2}^{min}\right)\cos(2\beta), & \beta \le \frac{\pi}{2} \\ N_{O2}^{min}, & \beta > \frac{\pi}{2}, \end{cases} \tag{36}$$

with the maximum O_2 column density $N_{O2}^{\max}$, the minimum O_2 column density $N_{O2}^{\min}$ and β being the angle to the subsolar point at Callisto (see Fig. 5). Fig. 6 shows an exemplary O_2 column density distribution according to expression (36).

The currently available observations of UV emission and electron density probe the day side and the terminator region of Callisto's atmosphere due to the geometrical constraints of the position of observing instruments and the position of Earth. As a consequence, we are not able to constrain the structure of the atmosphere ionosphere system at the night side. Therefore, we assume a constant column density for the night side atmosphere, expressly for $\beta > \pi/2$. Note that within this paper the minimum O_2 column density $N_{O2}^{\min}$ thus represents also the column density at the terminator and the maximum O_2 column density $N_{O2}^{\max}$ represents the column density at the subsolar point.

In summary, the two parameters $N_{O2}^{\max}$ and $N_{O2}^{\min}$ are the free variables which are varied to find the best O_2 atmosphere with respect to the available observations. We refer to

$$F_{as} = N_{O2}^{max}/N_{O2}^{min} \tag{37}$$

as the asymmetry factor of the O_2 atmosphere.

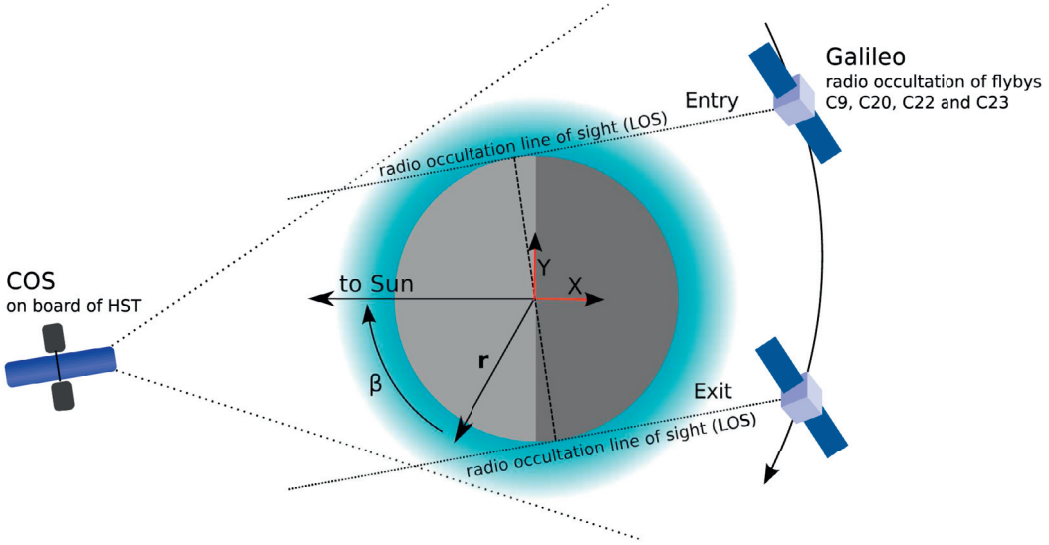

Fig. 5. Illustration of the observational geometries in Callisto's equatorial plane with sunlit and night side hemispheres illustrated with light and dark shades of gray; The blue shining area illustrates Callisto's atmosphere (here spherically symmetric); Illustration of the observational geometry of radio occultation and HST/COS observations (not true to scale); Definition of Sun orientated XY coordinate system within the equatorial plane of Callisto by red arrows; Definition of the subsolar angle β in terms of the atmosphere model for an arbitrary position vector $\boldsymbol{r}$. (For interpretation of the references to colour in this figure legend, the reader is referred to the web version of this article.)

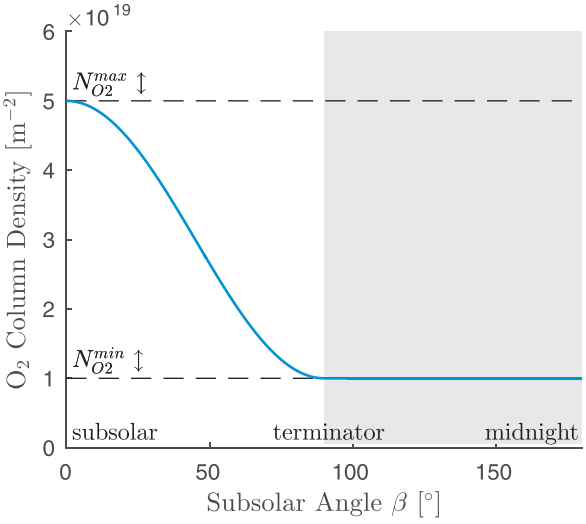

Fig. 6. O_2 column density distribution as a function of the subsolar angle β. N_{O2}^{max} and N_{O2}^{min} are variable model parameters, here they are exemplary set to $N_{O2}^{max} = 5 \times 10^{19}$ m^{-2} and $N_{O2}^{min} = 1 \times 10^{19}$ m^{-2}.

3.2. CO_2

The CO_2 part of Callisto's atmosphere is assumed to be spherically symmetric with a column density of $N_{CO2} = 0.8^{+0.48}_{-0.48} \times 10^{19}$ m^{-2} based on the observations of Carlson (1999). Since the nature of the CO_2 atmosphere is not sufficiently understood, we do not consider a spatial asymmetry. However, note that the Galileo spacecraft detected the signals of the CO_2 atmosphere when the spacecraft was close to the subsolar region during flyby C-10 (Carlson, 1999; Gurnett et al., 2000). Therefore, the terminator CO_2 column density might differ from the derived value.

3.3. H_2O

H_2O is expected to play a significant role within Callisto's atmosphere, too (Liang et al., 2005), although it has not been directly observed yet. In analogy to the approach of Liang et al. (2005), we assume that the H_2O part of Callisto's atmosphere follows the equilibrium vapor pressure relation above water ice with respect to the following constructed surface ice temperature distribution:

$$T(\beta) = \frac{1}{2}(T_{max} + T_{min}) + \frac{1}{2}(T_{max} - T_{min})\cos(\beta), \tag{38}$$

with the maximum surface ice temperature T_{max}, the minimum surface ice temperature T_{min} and β being again the angle to the subsolar point, thus neglecting thermal inertia.

The maximum and minimum surface ice temperatures are set by the surface temperature measurements of Voyager 2 (Hanel et al., 1979) with $T_{max} = 155$ K at the subsolar point and $T_{min} = 80$ K at midnight. The H_2O column density is then calculated using the expression for the equilibrium vapor pressure above water ice $P(T)$ (e.g., Murphy and Koop, 2005) according to the above defined temperature profile. Further we assume the atmosphere to be in thermal equilibrium with the surface ice temperature (isothermal in the vertical/radial direction). Hence, the H_2O column density distribution is given by

$$N_{H2O}(\beta) = \frac{P(T(\beta))\, H}{k_B T(\beta)}. \tag{39}$$

Fig. 7 shows the H_2O column density distribution together with the surface ice temperature distribution. Note that we neglect atmospheric transport, particularly neutral winds resulting from pressure gradients. The resulting H_2O atmosphere is highly asymmetric with a maximum around the subsolar point and an effectively frozen out H_2O atmosphere on the night side.

For low values of the investigated O_2 density parameter range, H_2O densities are significantly larger than O_2 densities in the subsolar region. As a consequence, the dominant ion species of the subsolar region will be likely H_3O^+ if we prescribe O_2 densities from the lower part of the explored parameter space. H_2O^+ would mainly react with H_2O yielding production of H_3O^+ as the associated reaction rate given by Huntress and Pinizzotto (1973) exceeds the reaction rate for H_2O^+ and O_2 forming O_2^+ given by Rakshit and Warneck (1980). The electron recombination rate for H_3O^+ is by a factor of ~ 1.5 larger than for O_2^+. The consideration of H_3O^+ is thus important for electron densities at locations close to the subsolar point. As we neglect the role of H_3O^+ ions, derived electron

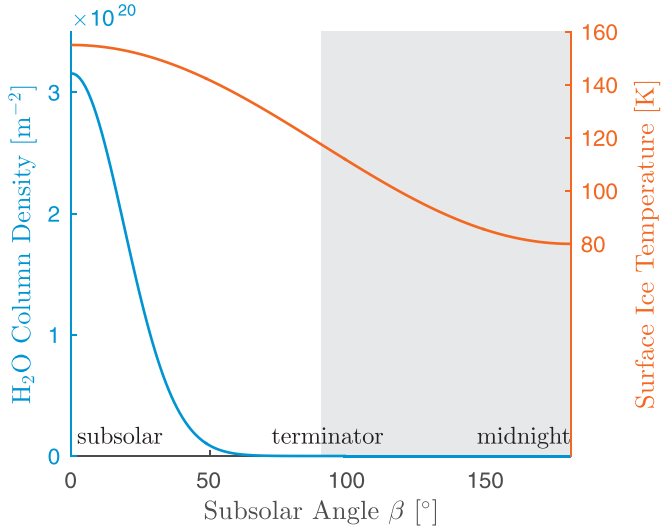

Fig. 7. Surface ice temperature distribution (red line) and H_2O column density distribution (blue line) as a function of the subsolar angle β with $T_{max} = 155$ K and $T_{min} = 80$ K. (For interpretation of the references to colour in this figure legend, the reader is referred to the web version of this article.)

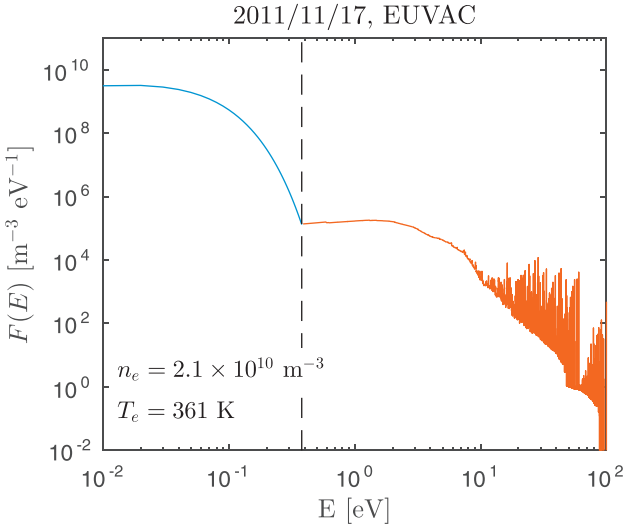

Fig. 8. Calculated electron energy distribution function of a volume element **without** H_2O. The prescribed neutral densities are: O_2 density $n_{n,1} = 1.0 \times 10^{15}$ m^{-3}, CO_2 density $n_{n,2} = 0.33 \times 10^{15}$ m^{-3}. Resulting electron density and temperature are $n_e = 2.1 \times 10^{10}$ m^{-3} and $T_e = 361$ K. The dashed black line marks the transition energy E_t, here: $E_t = 0.38$ eV.

densities will be overestimated by at most 25% around the subsolar point if the prescribed subsolar O_2 density is relatively minor. However, neglecting the role of H_3O^+ is only locally relevant close to the subsolar point. Therefore, this simplification will not affect later derived O_2 densities when we compare model results with observations, since electron density observations have probed the terminator regions where O_2^+ is the dominant ion species.

4. Results

In the following paragraphs, we first present electron energy distribution functions that solve the ionosphere model equations within given exemplary volume elements. Subsequently, we present the calculated electron densities, electron temperatures and UV emission intensities and compare them with the observations of Kliore et al. (2002) and Cunningham et al. (2015).

4.1. The electron energy distribution function

Our model shows that electron density and electron temperature significantly depend on the relative amount of H_2O in a given volume element of the atmosphere. Therefore, we present two exemplary electron energy distribution functions, one of a volume element without H_2O and one of a volume element with H_2O.

4.1.1. Electron energy distribution function without H_2O

Fig. 8 shows an exemplary electron energy distribution function of a volume element without any H_2O molecules. As long as the relative amount of H_2O is smaller than 4%, distribution function characteristics are fairly similar as in this presented case. The blue line shows the Maxwellian distribution of thermal electrons and the red line shows the distribution of suprathermal electrons. The dashed black line marks the transition energy E_t where the thermal and the suprathermal electron energy distribution functions have equal intensities. In this case the transition energy is 0.38 eV, the electron density of the thermal electrons is 2.1×10^{10} m^{-3} and the electron temperature is 361 K. Note that for later modeling results the transition energy is set to 1 eV since a variation of E_t within the range of 0.1 to 5 eV does not cause a significant change of the resulting electron density, electron temperature or UV emission intensity (see Appendix B and Hoegy (1984)).

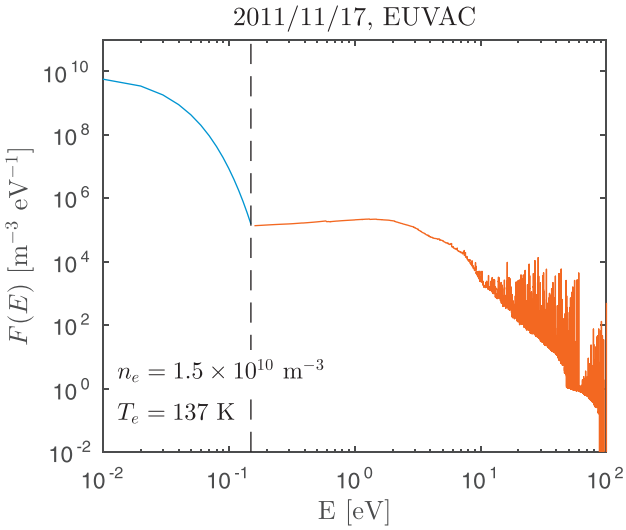

Fig. 9. Calculated electron energy distribution function of a volume element **with** a significant amount of H_2O. The prescribed neutral densities are: O_2 density $n_{n,1} = 1.0 \times 10^{15}$ m^{-3}, CO_2 density $n_{n,2} = 0.33 \times 10^{15}$ m^{-3} and H_2O density $n_{n,3} = 0.05 \times 10^{15}$ m^{-3}. Resulting electron density and temperature are $n_e = 1.5 \times 10^{10}$ m^{-3} and $T_e = 137$ K. Dashed black line marks the transition energy E_t.

The suprathermal electron energy distribution exhibits spikes with variations up to three orders of magnitude between some adjacent energy bins. These spikes result from the fact that our electron degradation scheme incorporates discrete production and loss processes. The effective electron production is dominated by the initial production from photoionization (see also Fig. 3). Therefore, the spikes of the calculated discrete photoelectron spectrum directly cause spike structures of the suprathermal electron energy distribution function. For energies smaller than 10 eV, the continuous energy loss due to electron electron collisions becomes significant causing a smoothing of the suprathermal distribution function.

4.1.2. Electron energy distribution function with H_2O

Fig. 9 shows an exemplary distribution function for a relative H_2O abundance of 5%. In comparison to the volume element with-

out H_2O presented above, the electron temperature is decreased by a factor of $\sim$ 0.4 to 137 K, the exact transition energy is decreased to 0.15 eV and the electron density is decreased by a factor of $\sim$ 0.7 to 1.5 $\times$ 10^{10} m^{-3}. Note again that increasing the transition energy artificially in this case to 1 eV would not significantly change the resulting electron density and electron temperature.

The difference between electron temperatures for volume elements with and without H_2O is caused by the cooling mechanism of thermal electrons due to rotational state excitation of H_2O molecules. Cross sections and resulting reaction rates for rotational state excitation are about 4 orders of magnitude larger for H_2O than for O_2 or CO_2 since H_2O molecules possess a large permanent magnetic dipole moment (e.g., Anzai et al., 2012; Demtröder, 2006). As a result, H_2O rotational cooling weakens or even compensates the heating of thermal electrons from Coulomb collisions with suprathermal electrons.

As a consequence of smaller electron temperatures, electrons within volume elements with H_2O recombine much faster and the resulting electrons to neutrals ratio is about 30% smaller than in volume elements without H_2O. This effect is anti-intuitive since we could expect an increase of electron density from adding more and more ionizable neutral particles to a volume element.

4.1.3. High energy part of the suprathermal electron energy distribution function

Within an optically thin atmosphere, the amplitude of the distribution function's high energy part ($>$ 10 eV) only weakly depends on the total neutral density n_n, since both production and degradation loss increase linearly with the neutral density almost negating each other. This behavior can directly be seen from Eq. (B.2) in the Appendix B. We can cancel out n_n from Eq. (B.2) if we introduce relative neutral abundances $\zeta_s = n_{n,s}/n_n$ and neglect processes that are not dominant at energies larger than 10 eV, namely, recombination with ions and electron electron collisions.

However, the amplitude of the distribution function depends significantly on the relative composition, namely, on the parameters ζ_s as a result of the different ionization cross sections of O_2, CO_2 and H_2O. For instance, O_2 dominated volume elements show $\sim$ 10% larger amplitudes than H_2O dominated ones and CO_2 dominated volume elements show $\sim$ 50% larger amplitudes than H_2O dominated ones.

From Eq. (33)–(35), we see that the atmospheric UV emission is sensitive to the amplitudes of the energy part above 14 eV. Therefore, the atmospheric composition seems to play an important role for the atmospheric UV emission of Callisto as one would expect from Fig. 3 of Wedlund et al. (2011) by comparison of the mean energy expended in collisions of electrons with O_2 and CO_2 gases.

4.2. Electron densities and comparisons with radio occultation results

First we show the spatial structure of the calculated electron densities for a spherically symmetric O_2 atmosphere and explain how the prescribed asymmetric H_2O distribution impacts the derived ionosphere. Then, we compare the calculated electron column densities along the radio occultation LOSs with the observational results of Kliore et al. (2002) and use this comparison to constrain the O_2 column density at the terminator N_{O2}^{min}.

4.2.1. The modeled ionospheric structure and the role of H_2O

Figs. 10 and 11 show calculated electron densities and electron temperatures of Callisto's ionosphere in the equatorial *XY*-plane for a spherically symmetric and optically thin O_2 atmosphere with $N_{O2}^{min} = N_{O2}^{max} = 3.0 \times 10^{19}$ m^{-2}. For a fixed altitude, electron densities have a maximum at the subsolar point and first decreases with an increasing subsolar angle β reaching a minimum at $\beta \approx$ 55°. For larger subsolar angles, electron densities increase again

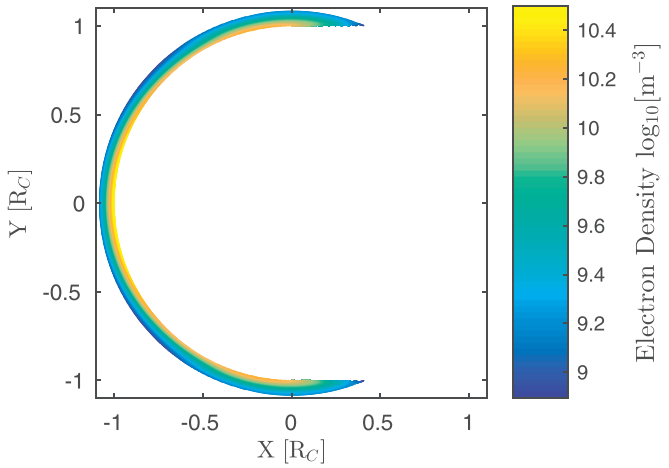

Fig. 10. Ionospheric electron densities in the equatorial plane. The Sun is shining from the -X direction. The prescribed atmosphere consists of a spherical O_2 atmosphere with a column density of 3.0 $\times$ 10^{19} m^{-2}, the CO_2 column density is 0.80 $\times$ 10^{19} m^{-2} and the H_2O atmosphere is incorporated as described by Eq. (39).

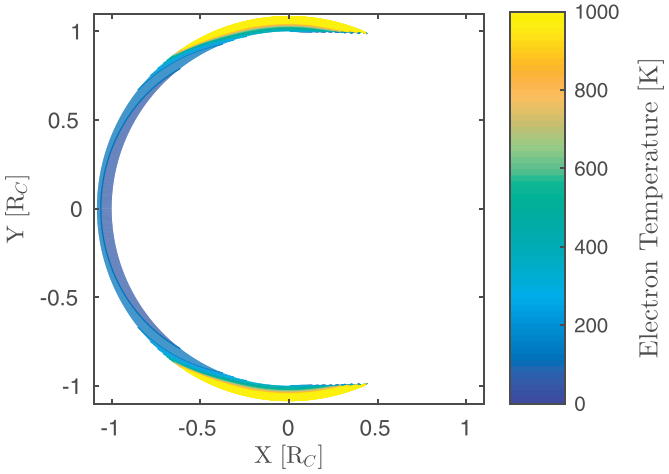

Fig. 11. Ionospheric electron temperatures in the equatorial plane. The atmospheric configuration is the same as in Fig. 10. The temperature range is limited to 0–1000 K in order to illustrate temperature variations at lower altitudes which are relevant for the model results. Electron temperatures exceed 1000 K reaching maximum values of $\sim$ 3000 K at higher altitudes in the terminator region.

and finally decrease to zero behind the terminator on the night side. The ionosphere also extents to the positive *X* hemisphere at higher altitudes where the line between atmosphere and Sun does not intersect Callisto. Calculated electron temperatures only weakly vary with varying prescribed O_2 densities. Therefore, the value range shown in Fig. 11 can be taken as a general result. In the terminator region, electron temperature are between 120 K and 1000 K within an altitude range of 60 km and increases up to $\sim$ 3000 K at 200 km. In the subsolar region, electron temperatures are between 120 K and 300 K within the investigated altitude range of 0–200 km.

The subsolar maximum and the electron density enhancement around the terminator result from the assumed asymmetric H_2O distribution. For $\beta \lesssim 55°$ the relative H_2O abundance is large enough that H_2O rotational state excitations cool down the thermal electrons to temperatures close to the assumed neutral temperature of 120 K (see Fig. 11). For $\beta \gtrsim 55°$ the relative H_2O abundance becomes sufficiently small so that H_2O rotational cooling is no longer that effective. As as result, the electron

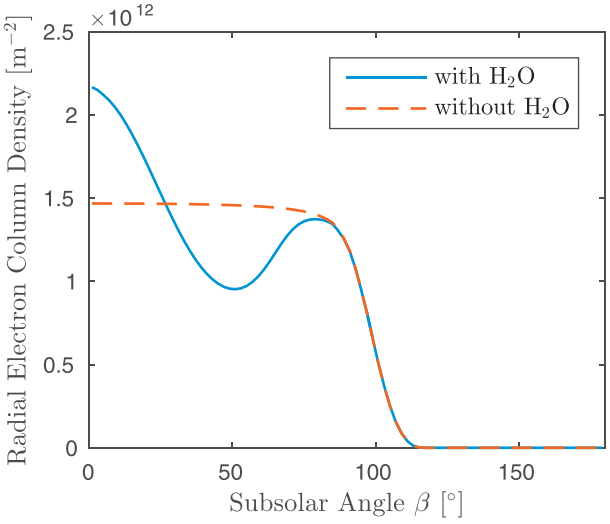

Fig. 12. Radial electron column densities as a function of the subsolar angle β for an atmosphere including H_2O (blue solid line) and without H_2O (red dashed line). For the blue model, the H_2O density distribution follows the water vapor pressure distribution as described by Eq. (39). For both models, the O_2 column densities are $N_{O2}^{max} = N_{O2}^{min} = 3.0 \times 10^{19}$ m^{-2} and the CO_2 column density is set to $N_{CO2} = 0.8 \times 10^{19}$ m^{-2}. (For interpretation of the references to colour in this figure legend, the reader is referred to the web version of this article.)

temperature increases, the recombination rate decreases and the electron density increases.

Fig. 12 shows radial electron column densities as a function of the subsolar angle β for both an atmosphere with the assumed H_2O distribution and without any H_2O at all. For $\beta \gtrsim 25°$, the increase of loss rates due to the inclusion of H_2O starts to dominate over the increase of electron production due to the inclusion of H_2O. In comparison to an atmosphere without H_2O, the inclusion of H_2O as an additional atmospheric species leads to approximately 12% smaller mean electron densities.

For the purpose of future modeling studies of Callisto's plasma environment and interpretations of observations, we derive the following approximated linear relation between the mean electron column density $\bar{N}_e$ and the O_2 column density N_{O2} of Callisto's atmosphere in case of a spherically symmetric O_2 distribution (including CO_2 and H_2O):

$$\overline{N}_e = 5.1 \times 10^{11}\ \text{m}^{-2} + 4.0 \times 10^{-9} N_{O2} \quad \text{for } N_{O2} < 3 \times 10^{20}\ \text{m}^{-2}. \tag{40}$$

The first term on the left hand side of Eq. (40) represents the mean electron column density originating from the water vapor pressure correlated H_2O density distribution and the spherically symmetric CO_2 atmosphere with $N_{CO2} = 0.8 \times 10^{19}$ m^{-2}. Note that the above fit is valid for a medium solar activity level comparable to the activity level during C-20, C-22, C-23 and the HST/COS observation from November 17th 2011.

4.2.2. Modeled and observed electron column densities along the LOSs of the Galileo radio occultation observations

In order to compare model results to radio occultation results, we have extracted LOS electron column densities of flybys C-9, C-20, C-22 and C-23 and associated observational errors from the radio occultation results of Kliore et al. (2002). For entries and exits of all flybys, Fig. 13 shows these radio occultation LOS electron column densities as black circles including error bars located at four LOS closest approach altitudes z_{int} (0, 25, 50, and 75 km). In each panel of Fig. 13, colored lines mark the corresponding LOS electron column densities derived from our ionosphere model. Each color is assigned to a certain prescribed atmospheric O_2 column density shown in the color scale on the right side of Fig. 13.

Our modeling shows that the discrepancy between entry and exit observations during C-22 and C-23 can be explained by a photoionization driven ionosphere as already mentioned by Cunningham et al. (2015). The entry tangential points are always slightly on the day side and the exit tangential points are always slightly on the night side. Therefore, the difference between entry and exit LOS electron column densities is a consequence of the photoionization driven asymmetric ionosphere around the terminator as well visible in Fig. 4 for flyby C-22.

While the observations show LOS electron column density peaks above Callisto's surface, the model results do not show such structures in the range of observed electron column density values. Strong peaks above Callisto's surface can be seen in the observational results of the entries of C-22 and C-23 as visible in Fig. 13 at $z_{int} = 25$ km and $z_{int} = 50$ km. For O_2 column densities up to 10^{21} m^{-2}, model results show that a photoionization driven ionosphere does not show comparable peak structures. Therefore, our results demonstrate that the observed peak structures are not caused by the simple combination of photoionization and an optically thick atmosphere as expected by Kliore et al. (2002). We will discuss this issue in more detail in Section 5.4. Note that the observational error ranges of the associated LOS electron column densities are relatively large with relative errors of 15–40%. Although our model does not reveal the observed peak structure, some atmospheric setups fit to the full set of observations within a 1σ error range as we will discuss in the following.

The calculated LOS electron column densities are not heavily affected by possible subsolar/terminator asymmetries of the O_2 atmosphere and, hence, depend basically on the O_2 column density at the terminator N_{O2}^{min}. In order to determine the terminator O_2 column density quantitatively from the radio occultation observations, we introduce a formal unbiased measure: the reduced Chi-Square parameter χ^2_{red} quantifying the goodness of fit between model results and observations. In case of $\chi^2_{red} \approx 1$ the deviation of the model prediction is in the same range as the observational error - the 1σ range. Atmosphere models with $\chi^2_{red} > 1$ imply inadequate fits between model and observations, while atmosphere models with $\chi^2_{red} \leq 1$ formally fit the observations within the error bars.

Assuming that the atmospheric density does not significantly vary at the terminator between different flybys, we derive that χ^2_{red} will be smaller than one if N_{O2}^{min} is smaller than 0.40×10^{19} m^{-2}. This O_2 column density is interpreted as an upper bound of the terminator O_2 column density. Note that this upper bound depends on the prescribed density of the CO_2 atmosphere. We do not focus on CO_2 column densities that are larger than the mean value given by Carlson (1999), since then the upper bound will become even smaller. For smaller prescribed CO_2 column densities, the upper bound increases. In analogy to Fig. 13, Fig. 14 shows the radio occultation LOS electron column densities for a prescribed CO_2 column density of $N_{CO2} = 0.32 \times 10^{19}$ m^{-2}, which is the lower bound of the observational error range of Carlson (1999). In this case, χ^2_{red} will be smaller than one if N_{O2}^{min} is smaller than 1.0×10^{19} m^{-2}. Therefore, the maximum terminator O_2 column density is $0.4^{+0.6} \times 10^{19}$ m^{-2} according to χ^2_{red} and considering the uncertainties of the CO_2 column density.

Note that from a statistical point of view, a pure CO_2 atmosphere with a column density of $N_{CO2} = 0.80 \times 10^{19}$ m^{-2} at the terminator also explains the radio occultation observations. Therefore, only based on the radio occultation observations, we cannot rule out an atmosphere with a dominant CO_2 abundance

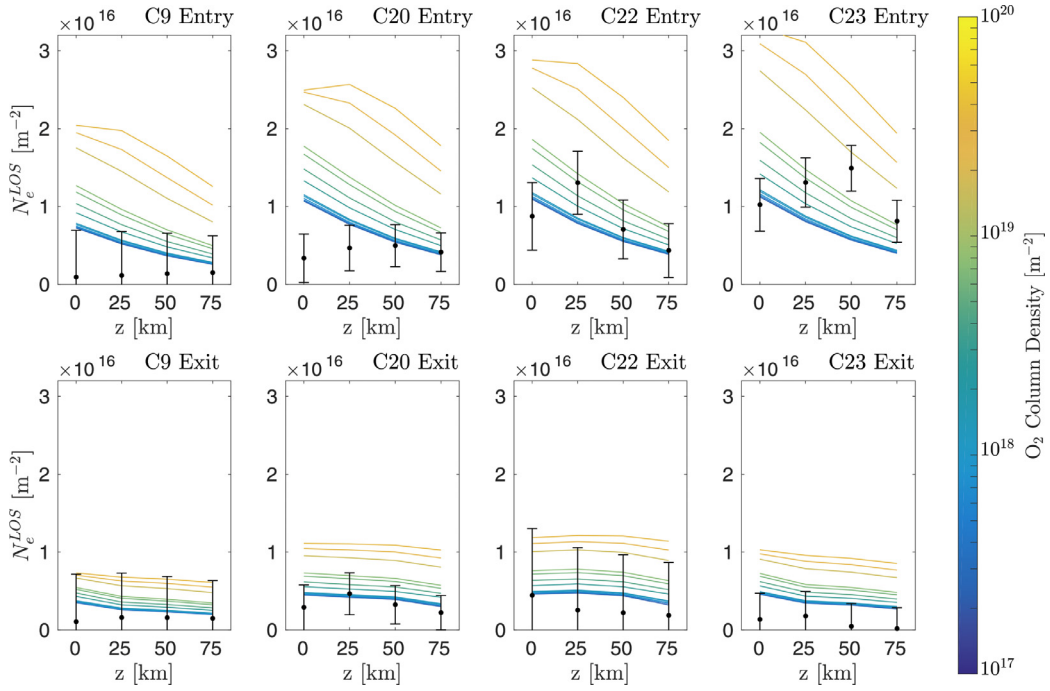

Fig. 13. Radio occultation LOS electron column densities of different closest approach altitudes. The prescribed CO_2 atmosphere is spherically symmetric with $N_{CO2} = 0.8 \times 10^{19}$ m^{-2} and H_2O is distributed as described by Eq. (39). Black circles with error bars represent radio occultation results extracted from Kliore et al. (2002), colored lines represent model results for spherically symmetric O_2 atmospheres with different column densities according to the color scale. (For interpretation of the references to colour in this figure legend, the reader is referred to the web version of this article.)

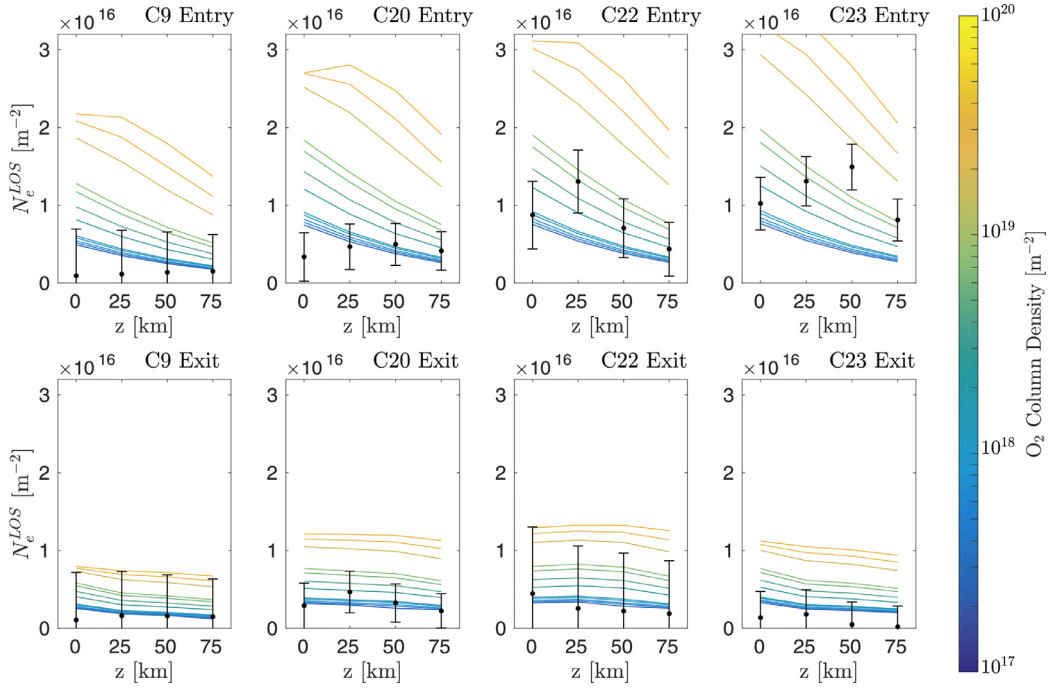

Fig. 14. Radio occultation LOS electron column densities of different closest approach altitudes as in Fig. 13. The CO_2 column density is set to $N_{CO2} = 0.32 \times 10^{19}$ m^{-2} and the H_2O column density is distributed as described by Eq. (39). (For interpretation of the references to colour in this figure legend, the reader is referred to the web version of this article.)

at the terminator but a sufficient subsolar O_2 abundance satisfying the HST/COS observations (see Section 4.3) but low enough O_2 densities in the terminator region not affecting electron densities. Although the fitting parameter analysis indicates a reasonable fit of model results and observations, a visual inspection of Fig. 13 and 14 still reveals some misfits. The peak structures during C-22 and C-23 and the outstanding low ionospheric signal during C-9 might indicate that the atmosphere ionosphere system possess dynamics which we do not cover with our model. Either electron transport or atmospheric dynamics might play an important role which could lead to provide an explanation of these differences. These questions will be discussed in more detail in Section 5.

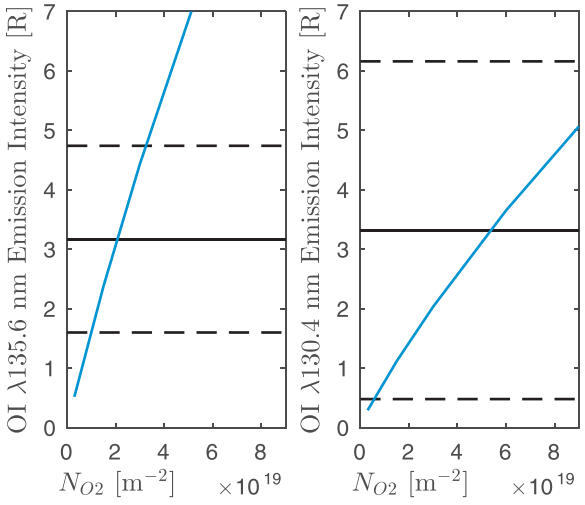

Fig. 15. Comparison of modeled atmospheric UV emission OI λ135.6 nm (left panel), OI λ130.4 nm (right panel) with observational constraints of Cunningham et al. (2015) as a function of O_2 column density assuming spherical symmetry of the O_2 atmosphere. Solid blue lines represent the model outcome, solid black lines mark the measured values by Cunningham et al. (2015), dashed lines mark the observational error range. (For interpretation of the references to colour in this figure legend, the reader is referred to the web version of this article.)

4.3. Modeled and observed atmospheric UV emissions intensities and comparisons with HST/COS observations

In this section we present derived UV emissions intensities for spherically symmetric O_2 atmospheres, where N_{O2}^{min} is equal to N_{O2}^{max}, and compare our model results with the HST/COS observations of Cunningham et al. (2015). In a second step, we then perform a combined comparison of model results with radio occultation and HST/COS observations.

4.3.1. Atmospheric UV emission from a spherically symmetric O_2 atmosphere

For spherically symmetric O_2 atmospheres, the comparison between model results and HST/COS observations implies an O_2 column density of $N_{O2} = 2.1^{+1.1}_{-1.1} \times 10^{19}$ m^{-2} on the basis of the OI λ135.6 nm emission line (see Fig. 15). This O_2 column density is 2–5 times larger than the maximum O_2 column density of $0.4^{+0.6} \times 10^{19}$ m^{-2} that we have derived from radio occultation observations. As we will discuss in Section 4.3.2, an atmospheric O_2 density gradient between subsolar and terminator region can possibly explain this difference. Note that the derived O_2 column densities correspond to an optically thin atmosphere.

The relation between the OI emission intensities and the O_2 column density is approximately linear. The linear behavior shown in Fig. 15 also shows that the upper part of the suprathermal electron energy distribution function is to some extend nearly independent of the total neutral density, at least for $N_{O2} < 3 \times 10^{20}$ m^{-2}. For larger O_2 column densities outside the range shown in Fig. 15, the characteristic of the derived OI λ135.6 nm emission experiences a saturation effect, which is due to the effect of optical depth. We extract the following fit between the O_2 column density and the brightness of the OI λ135.6 nm emission from Callisto's atmosphere for the purpose of future modeling work and interpretations of observations:

$$I_{135.6} = 1.51 \times 10^{-19} \text{ R m}^2 \; N_{O2} \quad \text{for } N_{O2} < 3 \times 10^{20} \text{ m}^{-2}. \qquad (41)$$

Note that this fit is valid for solar conditions similar to those prevailing on 17th of November 2011, the day of the HST/COS observation. The associated prescribed atmosphere also includes CO_2 with $N_{CO2} = 0.8 \times 10^{19}$ m^{-2} and H_2O as described by Eq. (39).

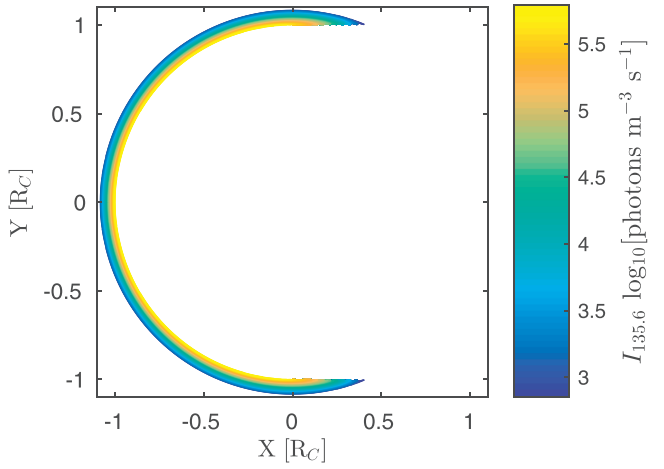

Fig. 16. UV emission intensity distribution in the equatorial plane. The Sun is shining from the -X direction. The prescribed atmosphere consists of a spherical O_2 atmosphere with a column density of 3.0×10^{19} m^{-2}, the CO_2 column density is 0.80×10^{19} m^{-2} and the H_2O atmosphere is incorporated as described by Eq. (39).

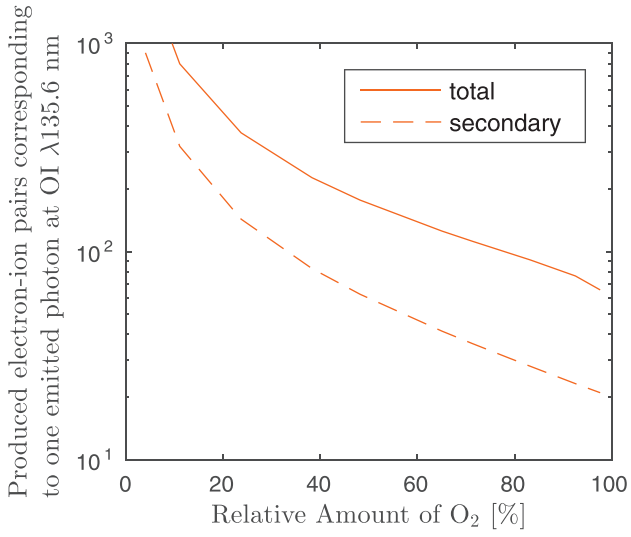

Fig. 17. Ratio between production rates of electron ion pairs and emission rate of OI λ135.6 nm photons as a function of the relative atmospheric O_2 abundance. The solid red line shows the ratio considering the total production rate and the dashed red line shows the ratio considering only secondary electron impact ionization. The derived mean O_2 column density of 2.1×10^{19} m^{-2} corresponds to a relative abundance of ~ 50%. (For interpretation of the references to colour in this figure legend, the reader is referred to the web version of this article.)

The spatial structure of the local UV emission intensity is shown in Fig. 16. As a consequence of the linear dependence on the O_2 density, the UV emission intensities decrease nearly exponentially with increasing altitude and have their maximum at the surface except at the night side. In the subsolar region, the UV emission intensity is slightly weakened due to the large subsolar H_2O column densities, which cause relatively large optical depths and roughly 10% smaller amplitudes of the electron energy distribution function at energies above 10 eV.

In analogy to the formulation in Cunningham et al. (2015), we calculate the relation between the rate of electron-ion pair production and the emission of one OI λ135.6 nm photon. We find that this ratio is variable and decreases with increasing O_2 column densities as shown in Fig. 17, where we set the numbers of electron-ion pairs in relation to the relative amount of atmospheric

O_2. The variation in this ratio is caused by the relative abundances of species, the total atmospheric abundance, and the fractional partitioning of solar EUV radiation into OI λ135.6 nm emission. For the derived O_2 column density of 2.1×10^{19} m^{-2}, there is one emitted OI λ135.6 nm photon per every 60 electron-ion pair produced by secondary ionization or per every 170 electron-ion pair produced by photoionization including secondary ionization. For increasing O_2 column densities these ratios converge to approximately one emitted OI λ135.6 nm photon per every 22 electron-ion pair produced by secondary ionization or per every 65 electron-ion pair produced by photoionization including secondary ionization.

The OI λ130.4 nm emission multiplet is only partially usable to constrain the O_2 abundance, since an important contribution to the OI λ130.4 nm emission might be produced from not only O_2, but also from atomic oxygen, CO_2, and H_2O. For all the latter species, the OI λ130.4 nm emission is brighter than their OI λ1356 nm emission intensities. We did not consider atomic oxygen since the density contribution of atomic oxygen is expected to be minor below an altitude of 100 km in comparison to O_2, CO_2 and H_2O (Liang et al., 2005). The calculated OI λ130.4 nm emission originating from O_2 can be roughly approximated by $I_{130.4} \approx I_{135.6}/2$ as a result of the ratio between the associated electron dissociation excitation cross sections. For the derived range of N_{O2}, the observed OI λ130.4 nm emission intensity agrees with our model results within the range of observational uncertainties. However, the uncertainties are relatively large and do not allow tight constraints on the atmospheric column densities of O_2 and O. If we neglect the uncertainties of the HST/COS observations, the observed ratio between OI λ135.6 nm and OI λ130.4 nm emissions will be approximately 1:1. An additional abundance of atomic oxygen with a relative abundance of 5–10% of the O_2 abundance might explain this 1:1 ratio. Note that this is a very rough estimation based on the ratios between OI λ130.4 nm and OI λ135.6 nm emission intensities of pure molecular and pure atomic oxygen taken from Cunningham et al. (2015): $I^{O2}_{130.4}/I^{O2}_{135.6} \approx 0.5$ and $I^{O}_{130.4}/I^{O}_{135.6} \approx 8.0$ including an averaged approximation of the non-linear resonance scattering effect for atomic oxygen.

We derive a HI λ121.6 nm disk averaged emission intensity below 1 R. Unfortunately, the Lyman-alpha emission from Callisto's atmosphere cannot easily be extracted from the observations, since the observed Lyman-α intensity is dominated by the reflected sunlight from Callisto's surface. Therefore, there is no available data which can be compared to our model results.

An interesting finding is that incorporating CO_2 and H_2O into our model reduces the resulting UV emission intensity of the atmospheric O_2 part by approximately 20%. This effect results from the impact of different neutral species on the upper energy regime of the electron energy distribution function. The electron energy distribution function is about 10% smaller in the upper energy regime for volume elements where H_2O is the dominant species, specially in the subsolar region. Since the composition of different species determines the ratio between production rate and degradation rate in the upper energy part, it plays an important role regarding the UV emission intensity.

4.3.2. Joint comparison of model results with HST/COS and radio occultation observations

At Callisto, we expect a denser O_2 atmosphere at the subsolar point than at the terminator due to the surface ice temperature dependence of sputtering and sublimation similar to the studies at Europa by Plainaki et al. (2012, 2013). In Section 3, we introduced a parametrized O_2 atmosphere model, which allows for an independent variation of the subsolar O_2 column density N^{max}_{02} and the terminator O_2 column density N^{min}_{02}. The O_2 column density of the sunlit hemisphere follows a cosine law as shown in Fig. 6.

The comparison of radio occultation results with model results shows that the radio occultation LOS electron column densities depend basically on the terminator O_2 column density N^{min}_{02} and only very weakly on the subsolar O_2 column density N^{max}_{02}. Therefore, we already know from the comparison of model results for spherically symmetric O_2 atmospheres with radio occultation observations that the terminator O_2 column densities N^{min}_{02} need to be smaller than $0.4^{+0.6} \times 10^{19}$ m^{-2}, also for the case of an asymmetric O_2 atmosphere.

According to this terminator O_2 column density range, we derive a possible subsolar O_2 column density range by comparing model results with the HST/COS observation. Fig. 18 shows the calculated UV emission intensity as a blue-green line as a function of N^{min}_{02} and N^{max}_{02}. Note that the scaling differs between the axes of N^{min}_{02} and N^{max}_{02}. The dark-blue and yellow lines mark the characteristics according to the lower and upper error boundaries of the HST/COS observation. The solid black line marks the derived upper bound of the terminator O_2 column density N^{min}_{02} from the comparison between model results and radio occultation observations. The gray area marks the possible combinations of N^{min}_{02} and N^{max}_{02} with respect to both the radio occultation observations of Kliore et al. (2002) and the HST/COS observation of Cunningham et al. (2015).

The model-observation comparison in Fig. 18 implies that Callisto's atmosphere very likely possesses a day night asymmetry. The prescribed O_2 atmosphere needs to be asymmetric with $N^{max}_{02} > N^{min}_{02}$ in order to explain HST/COS observations and radio occultation observations simultaneously. Only if both error bars on the observational constraints are included, we will find a single combination for which no asymmetry is required, namely, $N^{min}_{02} = N^{max}_{02} = 1.0 \times 10^{19}$ m^{-2}.

In order to estimate the asymmetry factor F_{as} of the O_2 atmosphere quantitatively using Eq. (37), we assume a terminator O_2 column density of 0.4×10^{19} m^{-2} according to the comparison of model results and radio occultation observation. For $N^{min}_{02} = 0.4 \times 10^{19}$ m^{-2} we calculate the possible range of N^{max}_{02} under the assumption of a CO_2 column density of 0.80×10^{19} m^{-2}. As a result, an asymmetry factor of $F_{as} = 15^{+9}_{-9}$ explains both observational constraints, where the error corresponds to the observational error range of the HST/COS observation. The associated subsolar O_2 column densities are in the range of $2.4 - 9.8 \times 10^{19}$ m^{-2}.

Note that the derived asymmetry factor is very sensitive to the assumed terminator CO_2 column density. A larger terminator CO_2 density requires less O_2 at the terminator to explain the observed electron densities. This implies a stronger day night asymmetry of the O_2 atmosphere, while terminator CO_2 densities smaller than the assumed value of 0.80×10^{19} m^{-2} lead to smaller O_2 asymmetries.

5. Discussion

We have developed a 3D-model of Callisto's photoionization driven ionosphere, which simultaneously calculates the spatial distribution of electron densities and atmospheric UV emission intensities from electron energy distribution functions. The model includes photoionization, secondary ionization, electron electron collisions and the energetically important collisions of electrons with neutrals and ions. The model is simplified as it does not consider electron and ion transport processes and does not describe the night side ionosphere since there have only been observations of the day side and the terminator region.

A comparison between model results and the HST/COS observations of Cunningham et al. (2015) implies an average O_2 column density of $2.1^{+1.1}_{-1.1} \times 10^{19}$ m^{-2}. This value is about one

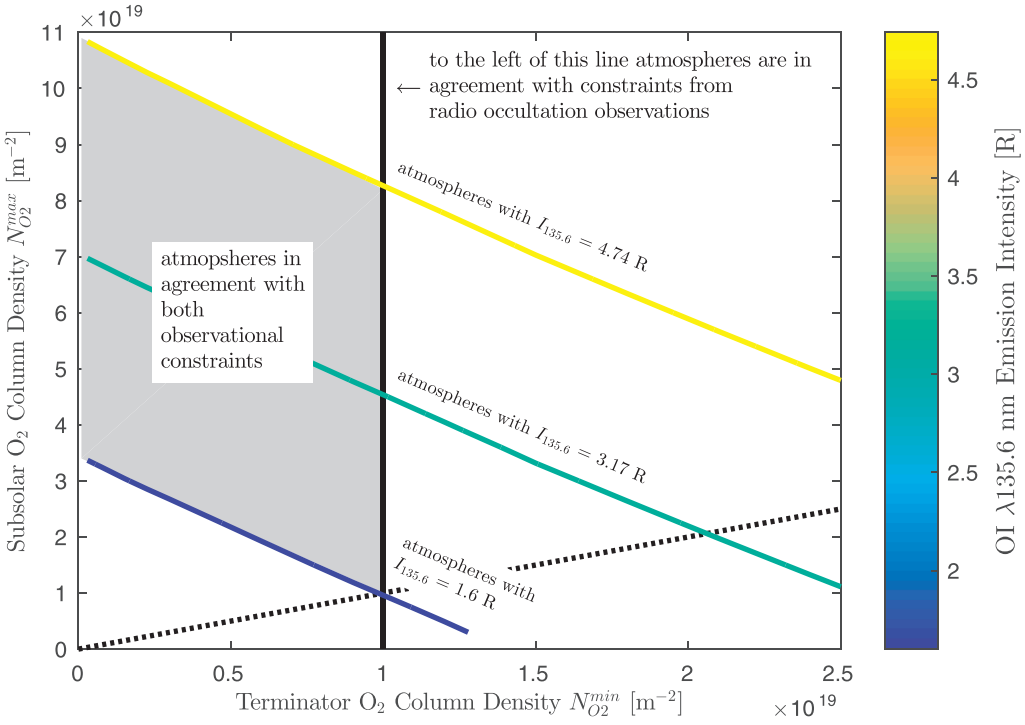

Fig. 18. Comparison of modeled atmospheric UV emission intensities with observational constraints of Cunningham et al. (2015) and Kliore et al. (2002). The prescribed asymmetric atmosphere is a function of two model parameters: the terminator O_2 column density N_{O2}^{min} (x-axis) and the subsolar O_2 column density N_{O2}^{max} (y-axis). The blue-green line identifies atmospheric configurations for which our model predicts UV emission intensities equal to the observational results of Cunningham et al. (2015), dark-blue and yellow lines show the corresponding lower and upper error range. The black solid line mark the upper bound of the terminator O_2 column density derived by the analysis of radio occultation observations with respect to all flybys and assuming the minimum CO_2 column density of 0.32×10^{19} m^{-2}. The dotted black line mark cases of spherically symmetric O_2 atmospheres. The gray area is the derived parameter space of N_{O2}^{min} and N_{O2}^{max} that agrees with both observational constraints with respect to the observational uncertainties. (For interpretation of the references to colour in this figure legend, the reader is referred to the web version of this article.)

order of magnitude smaller than the O_2 column density that was initially suggested by Kliore et al. (2002). However, our result is in fair agreement with the result of Cunningham et al. (2015), who derived an O_2 column density of $3.4^{+2.0}_{-1.8} \times 10^{19}$ m^{-2} from their HST/COS observations using a simpler model.

Further, a joint comparison of radio occultation and HST/COS observations with our model results indicates a subsolar/terminator asymmetric O_2 atmosphere. We are able to explain HST/COS observations and radio occultation observations simultaneously by prescribing a 15^{+9}_{-9} times larger O_2 column density at the subsolar point than at the terminator.

In order to evaluate the significances of our findings, the following open questions need to be addressed:

1. How can the neglect of electron and ion transport affect the ionospheric structure and change the interpretation regarding the atmospheric structure?
2. We assumed a constant and homogeneous scale height of 30 km for all atmospheric species. How will our model results be affected, if we assume the extreme case of decoupled scale heights for different species?
3. We neglect neutral winds which might be caused by the H_2O and O_2 density gradients between day and night side. What wind speeds are expected and how would a wind driven atmospheric redistribution affect our model results?
4. Our model cannot explain LOS electron column density peaks at higher altitudes. What are the reasons for this?
5. Are there hints for atmospheric variations with respect to the orbital phase as predicted for Europa by Plainaki et al. (2013) or due to variable rates of impinging magnetospheric ions?

5.1. The effect of neglecting electron transport

Our ionosphere model is based on the assumption that collisions of electrons with particles dominate over electron transport processes within Callisto's ionosphere. In order to evaluate this assumption, the following paragraphs contain a comparison of electron collision time scales and electron transport time scales.

We estimate the average collision time between electrons and neutrals by the mean flight time between two collisions:

$$\tau_{\mathrm{coll}}(\boldsymbol{r}, E) = (v_{\mathrm{e}}(E)\ n_n(\boldsymbol{r})\ \sigma_{tot}(E))^{-1}, \tag{42}$$

where v_e is the electron velocity, $n_n(\boldsymbol{r})$ the total neutral density at the location $\boldsymbol{r}$, and σ_{tot} the effective total cross section between electrons and the neutrals O_2, CO_2 and H_2O depending on the electron energy and the chemical composition of a volume element. For this discussion, we consider volume elements with the chemical composition of 50% O_2, 25% CO_2 and 25% H_2O according to the relations of the derived atmosphere. The electron velocity is approximated by the kinetic velocity $v_e(E) \approx \sqrt{2E/m_e}$. Regarding suprathermal electron collision time scales, Eq. (42) is evaluated for several electron energies: 0.1, 1, 10 and 50 eV. Regarding thermal electron collision time scales, Eq. (42) is evaluated using an energy of 0.1 eV (≙774 K).

To assess the role of ionospheric transport for the electron densities and UV emissions, we examine the time scales during which electrons are transported from the ionosphere out into the Jovian magnetosphere. In detail, transport time scales τ_{trans} are approximated by the ratio of appropriate length scales and the effective electron velocity. Transport time scales of suprathermal electrons are approximated by the ratio of Callisto's atmospheric scale height ($H \approx 30$ km) to the kinetic electron velocity v_e:

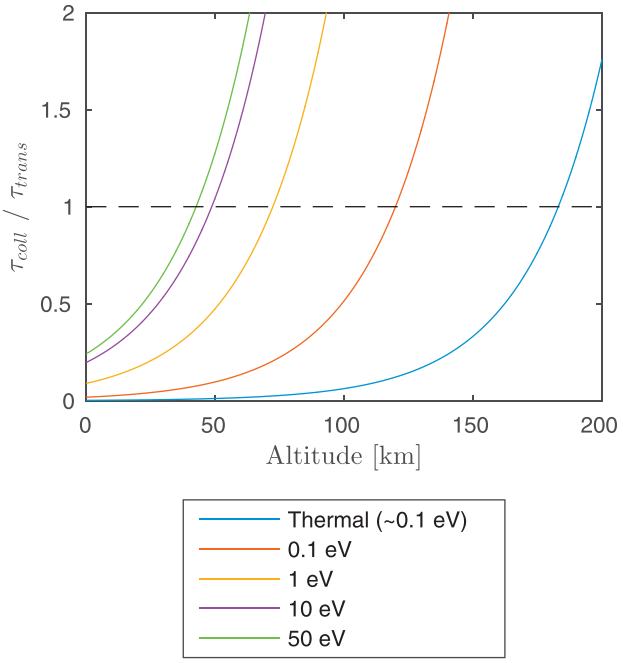

Fig. 19. Ratios between collision time scales and transport time scales $\tau_{\mathrm{coll}}/\tau_{trans}$ as a function of altitude using the approach for thermal electrons (blue line) and the approach for suprathermal electrons (other lines). The black dashed line denotes the limit where the collision time scales equal transport time scales.

$\tau_{trans}^{sup} = H/\sqrt{2E/m_e}$. For thermal electron transport time scales, we consider collective plasma effects. Here a distinction needs to be drawn between thermal electron transport along and perpendicular to the Jovian magnetic field. However, we will show that both transport time scales are approximately equal.

The perpendicular transport time scale is driven by the advection of the Jovian magnetospheric plasma. The advection time can be approximated by the ratio of Callisto's atmospheric scale height ($H \approx 30$ km) to the effective bulk plasma velocity of the magnetospheric plasma near the satellite. Close to Callisto, the magnetospheric plasma is likely strongly decelerated by a reduction factor α (Saur et al., 2002). We use a conservative approximation of this reduction factor with $\alpha \approx 0.1$ in agreement with (Strobel et al., 2002). Therefore, the perpendicular transport time scale is given by $\tau_{\perp} \approx H/v_{p,\,\mathrm{eff}} \approx 1.5$ s with $v_{p,\,\mathrm{eff}} \approx \alpha\, v_p$ and $v_p \approx 192$ km s^{-1} (Kivelson et al., 2004).

The parallel transport time scale of the thermal population is approximated by a typical length scale of the atmosphere ionosphere system, also the scale height $H \approx 30$ km, divided by the effective electron velocity parallel to the magnetic field. In principal, electrons can move freely parallel to the magnetic field, however, the electron motion is controlled by the ambient ions with one of the requirements being quasi-neutrality. Significant differences of electron and ion velocities will generate ambipolar electric fields which will tie electron and ion transport. Due to the large inertia of the ions, the effective parallel transport velocity is approximated by the mean ion velocity. Even though the ambipolar field will accelerate the ions to some extend, the ions are mainly accelerated by the electric field induced by the magnetospheric plasma flow. For the perpendicular transport a good approximation for newly generated ions is that they acquire a kinetic gyration velocity given by the local plasma velocity. The gyration velocity is initially perpendicular to the magnetic field. The resulting ion distribution function isotropizes subsequently. Therefore, a reasonable estimate for the parallel ion velocity is given by the local plasma velocity $v_{p,\,\mathrm{eff}} \approx \alpha\, v_p$. Thus parallel and perpendicular transport times are similar, i.e., $\tau_{\mathrm{trans}}^{\mathrm{therm}} \approx \tau_{\perp} \approx \tau_{\parallel} \approx 1.5$ s.

Fig. 19 shows ratios $\tau_{\mathrm{coll}(\boldsymbol{r})}/\tau_{trans}$ for a neutral column density of $\sim 3.5 \times 10^{19}$ m^{-2} with a neutral scale height of 30 km according to the findings of this study. Collision dominate over transport up to an altitude of ~ 45 km for suprathermal electrons and up to ~ 180 km for thermal electrons. For suprathermal electrons, we estimate the altitude limit of the local approximation conservatively for 50 eV electrons as the majority of photoelectrons ($\sim 95\%$) is produced at energies smaller than 50 eV (see, e.g., Fig. 3).

As a consequence, electron transport can lead to a substantial loss of ionospheric electrons above an altitude of ~ 45 km. Therefore, derived O_2 column densities might be underestimated. Note that the atmospheric volume below the altitude of 45 km contains $\sim 78\%$ of the total atmospheric mass. If we omit UV emissions and electron densities from above 45 km, our ionosphere model will need therefore 20%-30% larger O_2 column densities in order to meet the observational constraints.

The non-uniform nature of the transport effect could also play a role in shaping Callisto's ionosphere. After the deceleration of the magnetospheric plasma, the plasma is accelerated again when it is diverted around Callisto. Therefore, the plasma might reach peak velocities at the flanks of Callisto and minimum velocities above the upstream region. This difference can lead to an asymmetric distribution of the transport effect. However, a detailed discussion of these 3-D effects is out of the scope of this paper.

5.2. The atmospheric scale height

We assume that all atmospheric species have the same constant scale height of 30 km in order to keep the atmosphere model as simple as possible. However, different species can have different scale heights if atmospheric mixing through eddy diffusion is sufficiently weak. For the Earth we know that the mixing decreases with increasing altitude above the tropopause until the mesopause/lower thermosphere is reached. Up to now there is no study that constrains the atmospheric mixing and the extent of the homosphere at Callisto.

In order to evaluate the validity of our assumption we discuss the extreme case where each atmospheric species is in thermal equilibrium with the surface and do not interact with other species. The scale height is formally given by $H_s = k_B T/(m_s g_C)$, where T is the surface temperature, m_s is the mass of a molecule of the species s and g_C is the gravity acceleration at Callisto's surface. We neglect the altitude dependence of the gravity acceleration. The subsolar ($T = 155$ K) scale heights would be ~ 30 km for O_2, ~ 23 km for CO_2 and ~ 55 km for H_2O. All scale heights would be equally scaled by a factor of 3/4 at the terminator according to the assumed surface temperature distribution from Eq. (38).

These different scale heights would basically change our atmosphere model regarding the H_2O part. The H_2O abundance would be approximately doubled, since the prescribed H_2O column density is calculated as the product of the water vapor pressure equilibrium density at the surface and the assumed scale height. Such a density increase would increase the optical depth in the subsolar region, but the atmosphere would stay optically thin. The disk averaged UV emission intensity would slightly decrease since more volume elements would be H_2O dominated and the atmosphere would re-absorb a significant part of the UV emission ($> 5\%$) in the subsolar region. Further, the decline of LOS electron column densities with altitude will slightly increase if we set decoupled scale heights of 18 km for CO_2 and 23 km for O_2 at the terminator. However, we come to the conclusion that these effects do not change the model results significantly and do not lead to different interpretations.

5.3. Neutral winds and how they restrict atmospheric asymmetries

From our results we expect a significant density gradient of Callisto's atmosphere between day and night side. Here we estimate the resultant neutral wind speed v and sonic Mach number M_s.

The lifetimes of O_2 and CO_2 molecules are much longer than the lifetime of H_2O molecules, which have a sticking coefficient close to 1. In contrast to O_2 and CO_2, the production and loss processes of H_2O are expected to be faster than the transport processes. Therefore, we focus on the estimation of velocities of O_2 and CO_2 molecules regarding neutral winds.

We estimate the sonic Mach number as follows: We assume an one dimensional mass density distribution $\rho(x)$ of an ideal isotherm gas where the equation of state is $p = \rho c_s^2$ with the atmospheric pressure p and the sonic speed $c_s = \sqrt{\gamma k_B T_n / m_n}$. Due to the assumption of an isothermal atmosphere, the polytropic exponent is set to $\gamma = 1$. Further, m_n represents the neutrals' mass. From the Navier–Stokes equation

$$\frac{1}{\rho}\frac{dp}{dx} = -\frac{1}{2}\frac{d\left(v^2\right)}{dx} \tag{43}$$

we get the following conserved quantity:

$$v^2 + \frac{2}{\gamma}c_s^2 \log(\rho) = \text{cst.} \tag{44}$$

For a total O_2 and CO_2 mass density at the subsolar point ρ_{sub} and at the terminator ρ_{term}, the sonic Mach number M_s is then given by:

$$M_s^2 = \frac{2}{\gamma}\log\left(\frac{\rho_{sub}}{\rho_{term}}\right). \tag{45}$$

For Callisto, we estimate that neutral winds will become supersonic if the O_2 asymmetry factor F_{as} is larger than ~ 2.5. If the asymmetry factor decreases to 1.5, then wind speeds are driven with Mach numbers of about 0.6. In contrast, our comparison between model results and observations yields an asymmetry factor in the range of 6–24. The neutral winds will try to decrease atmospheric asymmetries generated by the atmospheric sources and sinks. Thus the winds make the lower values of our derived atmospheric asymmetries more likely compared to the large values.

We see three possible reasons why the real atmospheric asymmetry factor might be smaller than the one derived by our study. Firstly, if CO_2 column densities of the terminator region are smaller than the prescribed ones, the resulting asymmetry factor will be smaller, too, as already discussed in Section 4.3.2.

Secondly, we derive the asymmetry factor from radio occultation observations of the terminator region and HST/COS observations of the day side. These observations did not occur at the same time, there is a time gap of more than one decade between the HST/COS and the radio occultation observations and there is also a two years time gap between C-9 and C-23. Therefore, unknown and non-considered changes of the neutral atmosphere with time might play a role in interpreting the observations of Callisto's atmosphere ionosphere system. Concerning this matter, the possible effect of an O_2 density orbital phase dependency is discussed in Section 5.5.

Thirdly, if sufficient H_2O molecules are transported to the terminator region despite the sticking coefficient, electron densities will be smaller than predicted in the terminator region due to the electron cooling by rotational state excitation of H_2O. To meet the constraints of the radio occultation observations, the required O_2 terminator density increases in this case. As a consequence, assuming a redistribution of H_2O from the subsolar region to the terminator region yields result with a weaker atmospheric O_2 asymmetry.

5.4. LOS electron column density peaks above the surface

For the flybys C-22 and C-23 Kliore et al. (2002) derived that the electron density n_e reaches a maximum above the surface. To invert the observed line of sight electron column densities N_e^{LOS} obtained from the radio occultation technique into local electron densities n_e, Kliore et al. (2002) solved an Abel's integral equation assuming that the electron density distribution is spherically symmetric. This implies that if the electron density n_e has a maximum above the surface, the line of sight column density N_e^{LOS} needs to have a maximum above the surface, too.

An important aspect is that in all of the observations of Kliore et al. (2002) the radio line of sight is approximately parallel to the solar ray path. If a spherically symmetric neutral atmosphere falls of faster than $1/r$, the neutral line of sight column density N_n^{LOS} will have its maximum for rays grazing the surface. But N_n^{LOS} is never maximum for a ray path at higher altitudes. If N_n^{LOS} is maximal for a ray path just grazing the surface, then the optical depth is maximum for the ray path just grazing the surface, too. This implies that the total number of electrons produced by photoionization integrated along the solar ray path has its maximum for ray path just touching the surface. If we additionally assume that the recombination rate coefficient is spatially constant, the LOS electron column density is maximum also along the ray paths just grazing the surface in agreement with our model outcome. Only for very large prescribed O_2 densities, the actual deviation between the solar ray path and the radio line of sight causes electron column density peaks characteristics, which however misfit the observations (see, e.g, Fig. 13). Thus without transport of electrons, transport of electron energy (heat convection or heat conduction) and associated strongly inhomogeneous recombination rate coefficients, or multi-ion-chemistry effects, Callisto's electron density peaks above the surface in Kliore et al. (2002) cannot be explained.

Note that Cunningham et al. (2015) and Liang et al. (2005) compared locally calculated electron density altitude profiles at the terminator with the electron density altitude profiles of Kliore et al. (2002) neglecting the underlying assumption of a spherically symmetric ionosphere in Kliore et al. (2002) and found good agreement of model and observation. If we extract comparable altitude profiles at the terminator from our model outcome, these profiles will show peaks above the surface, too, very similar to those of Cunningham et al. (2015) and Liang et al. (2005). However, we have to stress that only modeled and observed radio occultation LOS electron column densities must be compared with each other.

Electron transport and the moon plasma interaction could play a role in creating LOS electron column density peaks above the surface as indicated by the results of Seufert (2012). The shape of the ionosphere might be modified by the interaction with the magnetospheric plasma. However, a detailed discussion of the effects of plasma dynamics is beyond the scope of this paper.

5.5. Possible time-variations of Callisto's atmosphere

Based on the radio occultation results, there are two factors that possibly introduce a variation of the atmospheric density with time: the angle between sunlight and plasma flow as suggested by Kliore et al. (2002) and the magnitude of the magnetospheric plasma flux.

If the atmospheric density varies between eastern and western elongation similar to what Plainaki et al. (2013) derived for Europa, we can explain why there was only a very weak ionosphere signal during flyby C-9. Assuming perfect corotation of the Jovian magnetospheric plasma at Callisto's orbit, Callisto's upstream side was sunlit during C-20, C-22, C-23 at western elongation while the downstream side was sunlit during C-9 at eastern elongation. Plainaki et al. (2013) calculated that the O_2 atmosphere at

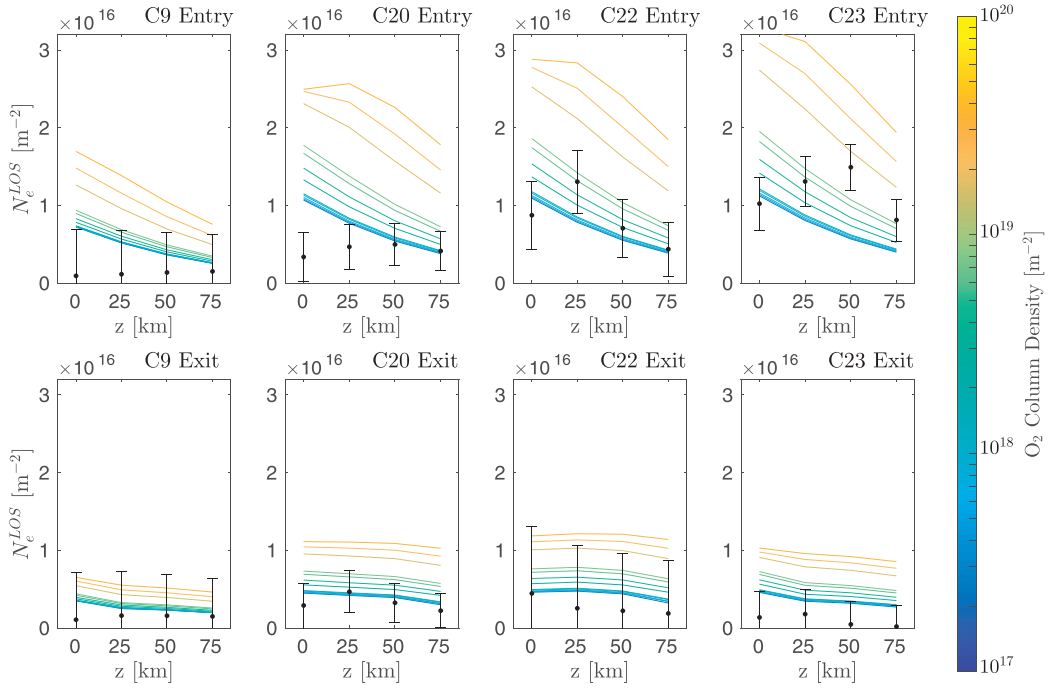

Fig. 20. Radio occultation LOS electron column densities of different closest approach altitudes as in Fig. 13. The atmospheric CO_2 column density is set to $N_{CO2} = 0.8 \times 10^{17}$ m^{-2} and H_2O is distributed as described by Eq. (39). The O_2 atmosphere is assumed to be 3 times denser during western elongation (C-20, C-22, C-23) than during eastern elongation (C-9). The given O_2 column densities refer to the western elongation column density, which means that prescribed O_2 column densities during C-9 are 3 times smaller than illustrated by the colored lines. (For interpretation of the references to colour in this figure legend, the reader is referred to the web version of this article.)

Europa is expected to be approximately 3-times denser at western elongation than at eastern elongation due to the temperature dependence of the sputtering efficiency. At western elongation, the majority of ambient energetic magnetospheric ions impinge on the sputtering efficient day side, while, at eastern elongation, only a minor portion of the energetic magnetospheric ions impinge on the sputtering efficient day side. If we apply these considerations to Callisto's atmosphere, the radio occultation results of C-9 will become more plausible.

Fig. 20 shows how the fitting between model results and radio occultation results will improve with respect to C-9 if the O_2 atmosphere is assumed to be 3 times denser during western elongation (C-20, C-22 and C-23) than during eastern elongation (C-9). The improved fit indicates that the low LOS electron column densities during C-9 are a result of the combination of smaller atmospheric densities and low solar activity (see Fig. 2). These considerations also agree with the speculations of Kliore et al. (2002) saying that efficient sputtering accompanied by photoionization can generate an ionosphere that is observable with radio occultation methods.

When Cunningham et al. (2015) observed UV emission from Callisto's atmosphere with HST/COS, Callisto was at about 15° east from the Sun-Jupiter line. At this position, approximately 40% of the day side hemisphere will overlap with the upstream side if we assume corotation of the magnetospheric plasma. Cunningham et al. (2015) reported also on earlier HST/COS observations that did not reveal any significant UV emission from Callisto's atmosphere. These observations were conducted when a smaller ratio of Callisto's day side hemisphere overlapped with the upstream side. Additionally, the solar photon flux was by a factor of 2 smaller in the EUV range during these earlier observations in comparison to the observation on the 17th of November 2011. Therefore, the available HST/COS observations also indicate that the atmospheric O_2 density might vary with the orbital phase and that the interplay of sputtering and photoionization is important for Callisto's atmosphere ionosphere system and its observability. In order to test the hypotheses of the orbital phase variability rigorously, further HST observations of Callisto are required, especially when Callisto is located at western elongation.

Magnetospheric variability is the second possible candidate for generating atmospheric O_2 density time-variations. The strongest ionospheric signal was detected during the entry of flyby C-23 when Callisto was close to the Jovian current sheet, a region of enhanced magnetospheric plasma particle flux (e.g., Seufert, 2012). An increased magnetospheric plasma particle flux can lead to an increase of the O_2 production rate via surface sputtering if it is accompanied by an increased energetic ion population as well. The effect on the atmosphere is non-linear because the atmospheric loss is affected by the plasma as well (e.g., Saur et al., 1998). The magnitude of the plasma particle flux is very variable at Callisto's orbit and has large uncertainties when extracted from the Galileo data (e.g., Seufert, 2012). From the limited set of available HST/COS observations, we however do not see a clear correlation between UV emission intensity and distance to the Jovian current sheet. Moreover, a detailed analysis of the role of the plasma transport requires also a proper description of Callisto's interaction with the upstreaming plasma.

6. Conclusions

The aim of this study is to constrain Callisto's atmospheric column densities and spatial structure based on available observations. For this purpose, we have used a local model for the electron energy distribution function at every location in Callisto's atmosphere to jointly explain the ionosphere observations by Kliore et al. (2002) and the UV emission observed by Cunningham et al. (2015). With our model we characterize the density and structure of the O_2-component in Callisto's atmosphere and the electron density. We derive an average O_2 column density

of $2.1^{+1.1}_{-1.1} \times 10^{19}$ m^{-2} in agreement with HST/COS observations of Cunningham et al. (2015). As a result, Callisto's atmosphere is expected to be optically thin. A subsolar/terminator asymmetric O_2 atmosphere with a maximum O_2 column density at the subsolar point significantly improves the synchronous fitting with the UV emission observation of Cunningham et al. (2015) and the electron density observation of Kliore et al. (2002). Our model predicts that the O_2 column density is about 0.4×10^{19} m^{-2} at the terminator and the associated subsolar O_2 column density is in the range of $2.4 - 9.8 \times 10^{19}$ m^{-2}. In fact, our analysis of the radio occultation observations of Kliore et al. (2002) shows that the terminator O_2 density could be in principle zero corresponding to an infinite subsolar/terminator asymmetry. However, under the consideration of neutral winds lower values of the derived O_2 asymmetries are much more likely than larger values. Therefore, it is very unlikely that the O_2 density vanishes at the terminator. We will find smaller asymmetries of the O_2 atmosphere if we prescribe smaller terminator CO_2 column densities according to the observational error range of the atmospheric CO_2 density from Carlson (1999).

Based on our results, we suppose that Callisto's O_2 atmosphere consists of a dense subsolar region driven by effective surface sputtering and a less dense terminator region, where surface sputtering is suppressed due to the lower surface ice temperatures. Comparisons between our model and radio occultation and HST/COS observations indicate that Callisto's atmospheric density varies with the orbital phase similar to what is expected at Europa (Plainaki et al., 2013).

Further we find that the detailed atmospheric composition crucially affects the suprathermal electron energy distribution function and the associated UV emission intensity. We calculate that on average one photon is emitted per every 170 electron ion pairs generated and per every 60 electron ion pairs produced by secondary electron impact ionization. The relative abundance of H_2O strongly affects the electron density. In contrast to the case of O_2 and CO_2 molecules, electron cooling by rotational state excitation of H_2O molecules plays an important role in the thermal electron energy range. If the relative abundance of H_2O is larger than 4%, this cooling mechanism leads to more rapid cooling of the thermal electrons leading to increased dissociative recombination and lower electron densities.

The current ionosphere model lacks the effect of electron transport and the interaction between Callisto and the upstreaming magnetospheric plasma. These factors might also play a role regarding atmospheric and ionospheric variations. Note that electron transport is affected by particle collisions and the electromagnetic field environment of Callisto, which is modified by the interaction of Callisto with the magnetospheric plasma.

Further HST observations, especially at western elongation, and in-situ and remote sensing observations by the JUICE spacecraft will help to understand and constrain Callisto's atmosphere ionosphere system in more detail.

Acknowledgements

This research was supported by the German Science Foundation (DFG) within the project 'Planetary Magnetism' (DFG-SPP 1488) and by the Graduate School of Geosciences (GSGS), Cologne. Two anonymous reviewers are thanked for critically reading the manuscript and suggesting substantial improvements. We thank the University of Colorado for the permission to use TIMED-SEE data. The numerical calculations have been performed on the CHEOPS cluster of the University of Cologne, Germany. We thank Dr. M. von Papen and A. Bloecker for reading a previous version of the manuscript and S. Kabanovic, A. Schreiner and F. Musacchio for very helpful discussions.

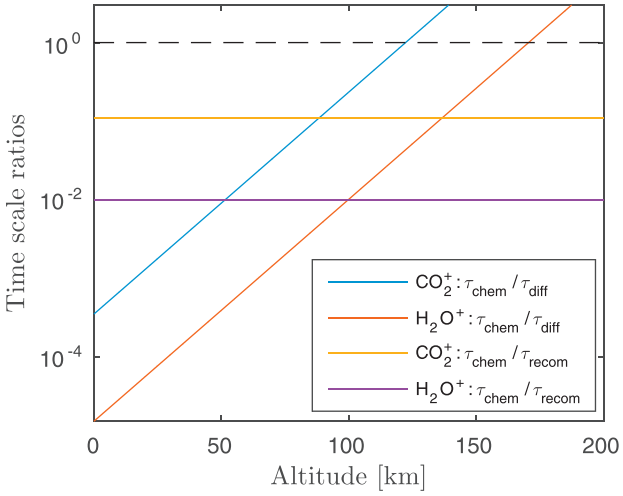

Fig. A1. Ion neutral loss time scales forming O_2^+ over ion diffusion time scales for CO_2^+ (blue line) and H_2O^+ (red line). Ion neutral loss time scales forming O_2^+ over recombination time scales for CO_2^+ (yellow line) and H_2O^+ (purple line). (For interpretation of the references to colour in this figure legend, the reader is referred to the web version of this article.)

Appendix A. Chemical reaction time scales

In order to evaluate the assumption that O_2^+ is the dominant ion species, we analyze time scales of chemical reactions of CO_2^+ and H_2O^+ with O_2 forming O_2^+. Fig. A.1 shows a comparison of associated ion-neutral loss time scales with ion transport (diffusion) time scales for CO_2^+ and H_2O^+. The chemical time scales are approximated using

$$\tau_{chem}^{CO2+} = [k_{c1}\ n_{O2}(z)]^{-1}, \tag{A.1}$$

$$\tau_{chem}^{H2O+} = [k_{c2}\ n_{O2}(z)]^{-1}, \tag{A.2}$$

with $k_{c1} = k(CO_2^+ + O_2 \rightarrow O_2^+ + CO_2) = 5.3 \times 10^{-17}$ $m^3\ s^{-1}$ (Copp et al., 1982), $k_{c2} = k(H_2O^+ + O_2 \rightarrow O_2^+ + H_2O) = 4.6 \times 10^{-16}$ $m^3\ s^{-1}$ (Rakshit and Warneck, 1980), $n_{O2}(z) = 0.7 \times 10^{15} \exp(-z/H)$ m^{-3} with the altitude z and the scale height H of 30 km, according to the findings of this study.

The ion diffusion time scale is estimated using

$$\tau_{diff} = \frac{H_i^2}{D_i} = \frac{k_B(T_i + T_e)\nu_{in}}{m_i g(z)^2} \approx 10^{-15} \frac{k_B(T_e + T_i)(R_C + z)^4}{G^2 M_C^2 m_i} n_n(z), \tag{A.3}$$

where we set the ion scale height H_i to the neutral scale height of 30 km, D_i denotes the ion diffusion coefficient, T_i the ion temperature and T_e the electron temperature which both are set to 300 K, m_i the ion mass, $g(z)$ the altitude dependent gravity acceleration, G the gravitational constant and M_C Callisto's mass: $M_C = 1.076 \times 10^{23}$ kg . The ion neutral collision frequency ν_{in} is set to $\nu_{in} = 1.0 \times 10^{-15}\ n_n(z)$ $m^3\ s^{-1}$ (Banks and Kockarts, 1973) with the neutral density altitude dependency $n_n(z) = 1.2 \times 10^{15} \exp(-z/H)$ m^{-3} according to the findings of this study.

Recombination time scales are estimated using

$$\tau_{recom}^{CO2+} = [k_{r1}\ n_e(z)]^{-1}, \tag{A.4}$$

$$\tau_{recom}^{H2O+} = [k_{r2}\ n_e(z)]^{-1}, \tag{A.5}$$

with $k_{r1} = k(CO_2^+ + e \rightarrow CO + O) = 3.8 \times 10^{-13}(T_e/300\ K)^{-0.5}$ $m^3\ s^{-1}$ (Brian and Mitchell, 1990), $k_{r2} = k(H_2O^+ + e \rightarrow OH + H + H) = 3.05 \times 10^{-13}(T_e/300\ K)^{-0.5}$ $m^3\ s^{-1}$ (Rosén et al., 2000),

$n_e(z) \approx 1.0 \times 10^{10} \exp(-z/H_e)$ m^{-3}, H_e the electron scale height which is set to the neutral scale height of 30 km and the electron temperature T_e approximated by 300 K.

For the major part of the atmosphere where O_2 is not expected to be significantly less dense than H_2O, the above estimation shows that the dominant ion is O_2^+ and the equilibrium of ion chemistry is reached sufficiently fast.

Appendix B. Solving for the electron energy distribution function

The numerical solution of the coupled Eqs. (1)–(5) is achieved in the following way: As a first step we approximate the ion density $n_{i,1}^{(0)}$ and the electron density $n_e^{(0)}$ by a simple chemical equilibrium model using a starting electron temperature of $T_e^{(0)} = 300$ K:

$$n_e^{(0)} = n_{i,1}^{(0)} = \sqrt{\frac{\sum_s \int_0^{E_{max}} P_{e,s}(E)\ \mathrm{d}E}{\alpha(T^{(0)})}}. \tag{B.1}$$

Using these first approximations of $n_{i,1}$ and n_e and a reasonable guess of the transition energy E_t in the order of $\sim$ 1 eV we can treat Eq. (1) as an inhomogeneous linear integral equation of type 2 in order to calculate the suprathermal electron energy distribution function $F_{\mathrm{sup}}^{(0)}(\mathrm{E})$. There is no general solution of this type of equation. Therefore, the method presented below is only valid for this specific problem.

For a fixed location, the solution of equation (1) is found recursively using

$$\begin{aligned} F_{\mathrm{sup}}^{(0)}(E) = \ & E^{-1/2} \left(n_e \sigma_{ee}(E, n_e, T_e) + n_{i,1} \sigma_{rec,1}(E) + \sum_s^{N_n} n_{n,s} \sum_{t_s=1}^{T_s} \sigma_{st_s}(E) \right)^{-1} \\ & \times \Bigg[\sum_s^{N_n} \Bigg(P_{e,s}(E) \sqrt{\frac{m_e}{2}} + n_{n,s} \int_{I_s}^{E_{max}} \mathrm{d}\tilde{E}\ \sqrt{E+\tilde{E}} \\ & \times \left(\sigma_{I,s}(E+\tilde{E}, E) + \sigma_{I,s}(E+\tilde{E}, \tilde{E}-I) \right) F(E+\tilde{E}) \\ & + n_{n,s} \sum_{t_s=1}^{T_s-1} \sqrt{E+\epsilon_{st_s}}\ \sigma_{st_s}(E+\epsilon_{st_s}) F(E+\epsilon_{st_s}) \Bigg) \\ & + n_e\ \sqrt{E+\Delta E}\ \sigma_{ee}(E, n_e, T_e)\ F(E+\Delta E) \Bigg]. \end{aligned} \tag{B.2}$$

Starting at the maximum energy $E_{\max}$ which photoelectrons can have, we subsequently calculate the number of electrons of the energy level below. Note that for a photoionization driven ionosphere an effective upper limit of $E_{\max}$ is given by the nature of the solar spectrum. The described procedure is possible since our model only considers degradation of suprathermal electrons to lower energy levels, as no acceleration processes are present.

Using the resulting distribution function we calculate all production and heating terms of the fluid (Eqs. (2)–(4)) according to Eqs. (6), (15)–(21), (30) and (31). The coupled non-linear fluid equations are solved numerically using a standard Newton-Method ensuring the quasi neutrality condition and yielding new electron densities $n_e^{(1)}$, ion densities $n_{i,1}^{(1)}$ and electron temperatures $T_e^{(1)}$.

We use this new set of $(n_e^{(1)},\ n_{i,1}^{(1)},\ T_e^{(1)})$ as new starting values to evaluate the suprathermal electron energy distribution function again. The whole process is repeated until the full set of variables $(F_{\mathrm{sup}}^{(k)}(E), n_{i,1}^{(k)}, n_e^{(k)}, T_e^{(k)})$ converges after several iteration steps when k becomes sufficiently large.

A second iteration process can then be applied varying the transition energy E_t until thermal and suprathermal electron energy distribution functions perfectly match at E_t. However, comprehensive tests have revealed that the macroscopic observables electron density, electron temperature and UV emission intensity are very robust with respect to the choice of the transition energy as expected from Hoegy (1984). Within the possible transition energy range of 0.1–5 eV, electron densities vary less than 2%, electron temperatures vary less than 5% and UV emission intensities vary less than 1%. Therefore, we choose a fixed transition energy of 1 eV for all volume elements to improve the computational performance.

For the calculation of the suprathermal electron energy distribution function, we choose an energy resolution of 0.01 eV as a trade-off of the smallest discrete energy loss $\epsilon_{\min}$ and the computational efficiency. For the purpose of computational performance, we approximate processes with an discrete energy loss smaller than 0.01 eV by an energy loss of 0.01 eV and a simultaneous rescaling of the associated cross sections according to the method of Swartz (1985). Rotational state excitation is treated in this way (see caption of Table 1).

The lower boundary of the simulation energy domain is set to E_t while the upper boundary of the simulated energy domain is set 100 eV since only a negligible amount of photoelectrons is produced at energies above 100 eV.

References

Allan, M., 1995. Measurement of absolute differential cross sections for vibrational excitation of o2 by electron impact. J. Phys. B 28 (23), 5163–5175. doi:10.1088/0953-4075/28/23/021.

Anzai, K., Kato, H., Hoshino, M., Tanaka, H., Itikawa, Y., Campbell, L., Brunger, M.J., Buckman, S.J., Cho, H., Blanco, F., Garcia, G., ao Vieira, P.L., Ingólfsson, O., 2012. Cross section data sets for electron collisions with H_2, O_2, CO, CO_2, N_2O and H_2O. Eur. Phys. J. D 66 (2), 1–8. doi:10.1140/epjd/e2011-20630-1.

Ashihara, O., Takayanagi, K., 1974. Velocity distribution of ionospheric low-energy electrons. Planet. Space Sci. 22 (8), 1201–1217. doi:10.1016/0032-0633(74)90005-1.

Banks, P.M., Kockarts, G., 1973. Aeronomy. Academic, San Diego, California.

Brian, J., Mitchell, A., 1990. The dissociative recombination of molecular ions. Phys. Rep. 186 (5), 215–248. doi:10.1016/0370-1573(90)90159-Y.

Butler, S.T., Buckingham, M.J., 1962. Energy loss of a fast ion in a plasma. Phys. Rev. 126 (1), 1–4. doi:10.1103/PhysRev.126.1.

Carlson, R.W., 1999. A tenuous carbon dioxide atmosphere on jupiter's moon callisto. Science 283 (5403), 820–821. doi:10.1126/science.283.5403.820.

Chen, R.H., Nagy, A.F., 1978. A comprehensive model of the venus ionosphere. J. Geophys. Res. 83 (A3), 1133–1140. doi:10.1029/JA083iA03p01133.

Copp, N.W., Hamdan, M., Jones, J.D.C., Birkinshaw, K., Twiddy, N.D., 1982. A selected ion flow tube study of the reactions of the gaseous ion CO_2^+ at 298 K. Chem. Phys. Lett. 88 (5), 508–511. doi:10.1016/0009-2614(82)83164-3.

Cravens, T.E., Korosmezey, A., 1986. Vibrational and rotational cooling of electrons by water vapor. Planet. Space Sci. 34 (10), 961–970. doi:10.1016/0032-0633(86)90005-X.

Cunningham, N.J., Spencer, J.R., Feldman, P.D., Strobel, D.F., France, K., Osterman, S.N., 2015. Detection of callisto's oxygen atmosphere with the hubble space telescope. Icarus 254, 178–189. doi:10.1016/j.icarus.2015.03.021.

Dalgarno, A., 1969. Inelastic collisions at low energies. Can. J. Chem. 47 (10), 1723–1729. doi:10.1139/v69-284.

Demtröder, W., 2006. Atoms, Molecules and Photons. Springer, Berlin, Heidelberg.

Famá, M., Shi, J., Baragiola, R.A., 2008. Sputtering of ice by low-energy ions. Surf. Sci. 602 (1), 156–161. doi:10.1016/j.susc.2007.10.002.

Gurnett, D.A., Persoon, A.M., Kurth, W.S., Roux, A., Bolton, S.J., 2000. Plasma densities in the vicinity of callisto from galileo plasma wave observations. Geophys. Res. Lett. 27 (13), 1867–1870. doi:10.1029/2000GL003751.

Hall, D.T., Strobel, D.F., Feldman, P.D., McGrath, M.A., Weaver, H.A., 1995. Detection of an oxygen atmosphere on jupiter's moon europa. Nature 373, 677–679. doi:10.1038/373677a0.

Hanel, R., Conrath, B., Flasar, M., Herath, L., Kunde, V., Lowman, P., Maguire, W., Pearl, J., Pirraglia, J., Samuelson, R., Gautier, D., Gierasch, P., Horn, L., Kumar, S., Ponnamperuma, C., 1979. Infrared observations of the jovian system from voyager 2. Science 206 (4421), 952–956. doi:10.1126/science.206.4421.952.

Hoegy, W.R., 1984. Thermal electron heating rate: a derivation. J. Geophys. Res. 89 (A2), 977–985. doi:10.1029/JA089iA02p00977.

Huntress, W.T., Pinizzotto, R.F., 1973. Product distributions and rate constants for ionmolecule reactions in water, hydrogen sulfide, ammonia, and methane. J. Chem. Phys. 59 (9), 4742–4756. doi:10.1063/1.1680687.

Hwang, W., Kim, Y.K., Rudd, M.E., 1996. New model for electronimpact ionization cross sections of molecules. J. Chem. Phys. 104 (8), 2956–2966. doi:10.1063/1.471116.

Itikawa, Y., 2002. Cross sections for electron collisions with carbon dioxide. J. Phys. Chem. Ref. Data 31 (3), 749–768. doi:10.1063/1.1481879.

Itikawa, Y., 2005. Cross sections for electron collisions with water molecules. J. Phys. Chem. Ref. Data 34 (1), 1–22. doi:10.1063/1.1799251.

Itikawa, Y., 2009. Cross sections for electron collisions with oxygen molecules. J. Phys. Chem. Ref. Data 38 (1), 1–20. doi:10.1063/1.3025886.

Jasperse, J.R., 1976. Boltzmann-fokker-planck model for the electron distribution function in the earth's ionosphere. Planet. Space Sci. 24 (1), 33–40. doi:10.1016/0032-0633(76)90058-1.

Jasperse, J.R., 1977. Electron distribution function and ion concentrations in the earth's lower ionosphere from Boltzmann-fokker-planck theory. Planet. Space Sci. 25 (8), 743–756. doi:10.1016/0032-0633(77)90126-X.

Johnson, R.E., 1990. Energetic Charged-particle Interactions with Atmospheres and Surfaces (Vol. 19). Springer, Berlin, Heidelberg.

Kanik, I., Noren, C., Makarov, O.P., Vattipalle, P., Ajello, J.M., 2003. Electron impact dissociative excitation of o_2: 2. absolute emission cross sections of the OI(130.4 nm) and OI(135.6 nm) lines. J. Geophys. Res. 108 (E11), 5126. doi:10.1029/2000JE001423.

Kivelson, M.G., Bagenal, F., Kurth, W.S., Neubauer, F.M., Paranicas, C., Saur, J., 2004. In: Bagenal, F., Dowling, T.E., McKinnon, W.B. (Eds.), Magnetospheric interactions with satellites in Jupiter: the planet, satellites and magnetosphere. Cambridge University Press, Cambridge, pp. 457–484.

Kliore, A.J., Anabtawi, A., Herrera, R.G., Asmar, S.W., Nagy, A.F., Hinson, D.P., Flasar, F.M., 2002. Ionosphere of callisto from galileo radio occultation observations. J. Geophys. Res. 107 (A11). doi:10.1029/2002JA009365. SIA 19-1–SIA 19-7

Liang, M.C., Lane, B.F., Pappalardo, R.T., Allen, M., Yung, Y.L., 2005. Atmosphere of callisto. J. Geophys. Res. 110 (E2), 1–9. doi:10.1029/2004JE002322.

Lindkvist, J., Holmström, M., Khurana, K.K., Fatemi, S., Barabash, S., 2015. Callisto plasma interactions: Hybrid modeling including induction by a subsurface ocean. J. Geophys. Res. 120 (6), 4877–4889. doi:10.1002/2015JA021212.

Liuzzo, L., Feyerabend, M., Simon, S., Motschmanmn, U., 2015. The impact of callisto's atmosphere on its plasma interaction with the jovian magnetosphere. J. Geophys. Res. 120 (11), 9401–9427. doi:10.1002/2015JA021792.

Makarov, O.P., Ajello, J.M., Vattipalle, P., Kanik, I., Festou, M.C., Bhardwaj, A., 2004. Kinetic energy distributions and line profile measurements of dissociation products of water upon electron impact. J. Geophys. Res. 109 (A9), 115. doi:10.1029/2002JA009353.

McGrath, M.A., Lellouch, E., Strobel, D.F., Feldmann, P.D., Johnson, R.E., 2004. In: Bagenal, F., Dowling, T.E., McKinnon, W.B. (Eds.), Satellites Atmospheres, in Jupiter: The planet, satellites and magnetosphere. Cambridge University Press, Cambridge, pp. 457–484.

Murphy, D.M., Koop, T., 2005. Review of the vapour pressures of ice and supercooled water for atmospheric applications. Q. J. R. Meteor. Soc. 131 (608), 1539–1565. doi:10.1256/qj.04.94.

Nagy, A.F., Banks, P.M., 1970. Photoelectron fluxes in the ionosphere. J. Geophys. Res. 75 (31), 6260–6270. doi:10.1029/JA075i031p06260.

Opal, C.B., Peterson, W.K., Beaty, E.C., 1971. Measurements of secondary-electron spectra produced by electron impact ionization of a number of simple gases. J. Chem. Phys. 55 (8), 4100–4106. doi:10.1063/1.1676707.

Peverall, R., Rosén, S., Peterson, J.R., Larsson, M., Al-Khalili, A., Vikor, L., Semaniak, J., Bobbenkamp, R., Padellec, A.L., Maurellis, A.N., van der Zande, W.J., 2001. Dissociative recombination and excitation of $o2^+$: cross sections, product yields and implications for studies of ionospheric airglows. J. Chem. Phys. 114 (15), 6679–6689. doi:10.1063/1.1349079.

Plainaki, C., Milillo, A., Mura, A., Orsini, S., Massetti, S., Cassidy, T., 2012. The role of sputtering and radiolysis in the generation of europa's exosphere. Icarus 218 (2), 956–966. doi:10.1016/j.icarus.2012.01.023.

Plainaki, C., Milillo, A., Mura, A., Saur, J., Orsini, S., Massetti, S., 2013. Exospheric o_2 densities at europa during different orbital phases. Planet. Space Sci. 88, 42–45. doi:10.1016/j.pss.2013.08.011.

Rakshit, A.B., Warneck, P., 1980. Reactions of CO_2^+, $CO_2CO_2^+$ and h_2o^+ ions with various neutral molecules. J. Chem. Soc., Faraday Trans. 2 76, 1084–1092. doi:10.1039/F29807601084.

Rees, M.H., 1989. Physics and Chemistry of the Upper Atmosphere. Cambridge University Press, Cambridge.

Retherford, K.D., Moos, H.W., Strobel, D.F., Wolven, B.C., Roesler, F.L., 2000. Io'S equatorial spots: Morphology of neutral UV emissions. J. Geophys. Res. 105 (A12), 27157–27165. doi:10.1029/2000JA002500.

Richards, P.G., Fennelly, J.A., Torr, D.G., 1994. EUVAC: A solar EUV flux model for aeronomic calculations. J. Geophys. Res. 99 (A5), 8981–8992. doi:10.1029/94JA00518.

Rosén, S., Derkatch, A., Semaniak, J., Neau, A., Al-Khalili, A., Padellec, A.L., Viktor, L., Thomas, R., Danared, H., Ugglas, M.a., Larsson, M., 2000. Recombination of simple molecular ions studied in storage ring: dissociative recombination of h_2o^+. Faraday Discuss. 115, 295–302. doi:10.1039/A909314A.

Roth, L., Saur, J., Strobel, D.F., Feldman, P.D., McGrath, M.A., Nimmo, F., 2014. Transient water vapor at europa's south pole. Science 343 (6167), 171–175. doi:10.1126/science.1247051.

Saur, J., Duling, S., Roth, L., Jia, X., Strobel, D.F., Feldman, P.D., Christensen, U.R., Retherford, K.D., McGrath, M.A., Musacchio, F., Wennmacher, A., Neubauer, F.M., Simon, S., Hartkorn, O., 2015. The search for a subsurface ocean in ganymede with hubble space telescope observations of its auroral ovals. J. Geophys. Res. 120 (3), 1715–1737. doi:10.1002/2014JA020778.

Saur, J., Neubauer, F.M., Strobel, D.F., Summers, M.E., 2000. Io'S ultraviolet aurora: remote sensing of io's interaction. Geophys. Res. Lett. 27 (18), 2893–2896. doi:10.1029/2000GL003824.

Saur, J., Neubauer, F.M., Strobel, D.F., Summers, M.E., 2002. Interpretation of galileo's io plasma and field observations: I0, i24, and i27 flybys and close polar passes. J. Geophys. Res. 107 (A12). doi:10.1029/2001JA005067. SMP 5-1–SMP 5–18

Saur, J., Strobel, D.F., Neubauer, F.M., 1998. Interaction of the jovian magnetosphere with europa: constraints on the neutral atmosphere. J. Geophys. Res. 103 (E9), 19947–19967. doi:10.1029/97JE03556.

Schunk, R., Nagy, A.F., 2009. Ionospheres: Physics, Plasma Physics, and Chemistry. Cambridge University Press, Cambridge.

Schunk, R.W., Nagy, A.F., 1978. Electron temperatures in the f region of the ionosphere: Theory and observations. Rev. Geophys. 16 (3), 355–399.

Seufert, M., 2012. Callisto: Induction Signals, Atmosphere and Plasma Interaction, Dissertation. University of Cologne.

Sheehan, C.H., St Maurice, J.-P., 2004. Dissociative recombination of n2+, o2+, and NO+: Rate coefficients for ground state and vibrationally excited ions. J. Geophys. Res. 109 (A3), A03302. doi:10.1029/2003JA010132.

Stamnes, K., Rees, M.H., 1983. Inelastic scattering effects on photoelectron spectra and ionospheric electron temperature. J. Geophys. Res. 88 (A8), 6301–6309. doi:10.1029/JA088iA08p06301.

Strickland, D.J., Bishop, J., Evans, J.S., Majeed, T., Shen, P.M., Cox, R.J., Link, R., Huffman, R.E., 1999. Atmospheric ultraviolet radiance integrated code (AURIC): Theory, software architecture, inputs, and selected results. J. Quant. Spectrosc. Radiat. Transfer 62 (6), 689–742. doi:10.1016/S0022-4073(98)00098-3.

Strobel, D.F., Saur, J., Feldman, P.D., McGrath, M.A., 2002. Hubble space telescope space telescope imaging spectrograph search for an atmosphere on callisto: A jovian unipolar inductor. Astrophys. J. 581 (1), L51–L54. doi:10.1086/345803.

Swartz, W.E., 1985. Optimization of energetic electron energy degradation calculations. J. Geophys. Res. 90 (A7), 6587–6593. doi:10.1029/JA090iA07p06587.

Swartz, W.E., Nisbet, J.S., Green, A.E.S., 1971. Analytic expression for the energy-transfer rate from photoelectrons to thermal-electrons. J. Geophys. Res. 76 (34), 8425–8426. doi:10.1029/JA076i034p08425.

Takayanagi, K., Itikawa, Y., 1970. The rotational excitation of molecules by slow electrons. Adv. Atomic Mol. Phys. 6, 105–153. doi:10.1016/S0065-2199(08)60204-3.

Vorburger, A., Wurz, P., Lammer, H., Barabash, S., Mousis, O., 2015. Monte-carlo simulations of callistos exosphere. Icarus 262, 14–29. doi:10.1016/j.icarus.2015.07.035.

Wedlund, C.S., Gronoff, G., Lilensten, J., Mnager, H., Barthlemy, M., 2011. Comprehensive calculation of the energy per ion pair or w values for five major planetary upper atmospheres. Annales Geophysicae 29 (1), 187–195. doi:10.5194/angeo-29-187-2011.

Yung, Y.L., McElroy, M.B., 1977. Stability of an oxygen atmosphere on ganymede. Icarus 30 (1), 97–103. doi:10.1016/0019-1035(77)90124-5.